Guided moments formalism: A new efficient full-neutrino treatment for astrophysical simulations

M. R. Izquierdo, F. Abalos, and C. Palenzuela

Departament de Física, Universitat de les Illes Balears, Palma de Mallorca, E-07122, Spain and Institute of Applied Computing and Community Code (IAC3), Universitat de les Illes Balears, Palma de Mallorca, E-07122, Spain

(Received 21 December 2023; accepted 30 January 2024; published 26 February 2024)

We present the new guided moments (GM) formalism for neutrino modeling in astrophysical scenarios like core-collapse supernovae and neutron star mergers. The truncated moments approximation (M1) and Monte-Carlo (MC) schemes have been proven to be robust and accurate in solving the Boltzmann equation for neutrino transport. However, it is well known that each method exhibits specific strengths and weaknesses in various physical scenarios. The GM formalism effectively solves these problems, providing a comprehensive scheme capable of accurately capturing the optically thick limit through the exact M1 closure and the optically thin limit through an MC-based approach. In addition, the GM method also approximates the neutrino distribution function with a reasonable computational cost, which is crucial for the correct estimation of the different neutrino-fluid interactions. Our work provides a comprehensive discussion of the formulation and application of the GM method, concluding with a thorough comparison across several test problems involving the three schemes (M1, MC, GM) under consideration.

DOI: 10.1103/PhysRevD.109.043044

I. INTRODUCTION

The coalescence of neutron stars is an extraordinary phenomenon in high-energy astrophysics, occurring in extreme environments marked by strong self-gravity, high densities, and elevated temperatures. The simultaneous detection of gravitational waves (GWs) and electromagnetic (EM) signals from binary neutron stars, exemplified by the ground-breaking GW170817 event [1,2], shows the potential of multimessenger astronomy. Numerous detections of GWs and EM signals from neutron star mergers are expected in the coming years (see, for instance, [3]). The observation of such signals is predicted to have a profound impact on both astrophysics and fundamental physics. Nevertheless, the complexity of modeling all of the involved physical interactions constrains our capacity to realistically simulate these binary mergers and compare them with present observations. Unraveling the physics embedded in these signals requires solving, at least approximately, the general-relativistic radiation magnetohydrodynamic equations: the Einstein equations for depicting strong gravity, relativistic magnetohydrodynamics to model magnetized fluids, and the Boltzmann equation to describe the production and transport of neutrinos. Obtaining accurate solutions for these equations, in realistic general astrophysical settings like neutron star mergers, is an exceedingly challenging task which can solely be addressed through numerical simulations.

After the merger, a massive neutron star or a black hole, surrounded by a strongly magnetized hot and dense accretion torus, is likely to be formed (see, for instance, [4,5]). Throughout the coalescence, various regions may experience conditions ranging from the *optically thin regime*, characterized by freely streaming neutrinos, to the *optically thick regime*, where neutrinos are mostly trapped and propagate through diffusion. Due to their substantial energies and luminosities, neutrinos are expected to play a fundamental role in physical processes in the postmerger phase of a neutron star merger (for an extensive review, see [5]). In particular, neutrino interactions are expected to induce changes in matter composition, influencing the conditions relevant to the *r*-process nucleosynthesis (e.g., [6–9]). Neutrinos produced in hot and dense matter regions will diffuse and eventually decouple from the fluid at lower densities, being emitted from the system while carrying away energy. As neutrinos extract energy from the system, they could give rise to additional matter outflows, manifested as neutrino-driven winds (e.g., [10–13]).

Accurately capturing all of these phenomena in neutron star merger simulations requires an accurate and realistic treatment of neutrino transport in numerical relativity codes [14]. This task involves the tremendous challenge of solving the seven-dimensional Boltzmann equation, which describes the evolution of a distribution function for each neutrino species. To address this complexity, several approaches, including direct and approximate methods, have been explored. Presently, various methods directly attempt to solve the full Boltzmann equation in full general relativity, using Monte Carlo (MC)-based approaches (see, for example, [15–23]), lattice-Boltzmann

methods [24], expansion of momentum-space distributions into spherical harmonics (P_n) methods (see, e.g., [25–27]), discrete-ordinates (S_n) methods (see, e.g., [28–30]), and a finite-element approach in angle [31]. Direct methods, although expected to converge to the true solution, often present challenges in their implementation and computational cost, making them in most cases impractical for providing a numerical solution with sufficient accuracy. A notable example is the handling of the optically thick regime in the MC-based methods, where resolving the small neutrino mean free path becomes challenging, often requiring further simplifications (see, for instance, [5,16,18,21,32–35]).

On the other hand, approximate methods strike a balance between accuracy and computational efficiency. Neutrino leakage schemes (see, for example, [36–43]) are a widely used approach due to their computational inexpensiveness. However, the absence of neutrino reabsorption may lead, in certain scenarios, to crude estimations in the amount and composition of the ejecta. A more sophisticated approximation, known as the truncated moment formalism [44,45], involves the evolution of the lowest moments of the neutrino distribution function (see, e.g., [46–61]). Typically, only the first two moments are evolved, such that it is often referred to as the M1 scheme. This approach requires an algebraic closure for computing the higher moments, which is only known in some limit cases. Additionally, the evolution system can be simplified significantly by deriving evolution equations for the energy-integrated moments, transforming the seven-dimensional Boltzmann equation into a $3+1$ system that resembles the hydrodynamic equations. Unfortunately, even in this simplified scenario, numerical and mathematical challenges persist. Specifically, the truncated moment equations may contain potentially stiff source terms arising from neutrino-matter interactions, causing the equations to shift from hyperbolic to parabolic type in optically thick regions. While this issue can be addressed by employing an implicit-explicit Runge-Kutta (IMEX) time integrator ([62–65]), achieving a balance between accuracy and stability remains a critical consideration (for more details about IMEX schemes within the M1 formalism, we refer to [56,58]). Additionally, moment-based schemes may produce unphysical shocks in regions where radiation beams intersect, leading to solutions that differ from the true solutions of the Boltzmann equation (see, for instance, the discussion in [5]).

In this work, we introduce the *guided moments* (GM) formalism, inspired in the seminal work presented in [18] and the *moment-guided MC method* developed in [66,67]. Our approach exploits the benefits of the approximate truncated moment formalism, incorporating evolution equations similar to those in hydrodynamics and ensuring accuracy in the optically thick regime. Additionally, it incorporates aspects of the MC method, providing convergence to the exact solution and accuracy in the optically thin regimes. By exploiting the advantages of each method, we overcome their individual limitations. In this context, we combine the M1 and MC approaches to enhance the overall efficacy of our formalism. The fundamental idea is to close the M1 evolution equations by computing the second moment with information from the MC solution, especially in the optically thin regime where the M1 closure is not exact. In contrast, an exact analytical closure for the second moment exists in the optically thick limit, such that the M1 formalism can provide a more accurate and cost-effective solution than the one obtained from the MC scheme, which suffers in this regime. A suitable projection of the MC distribution function, such that the MC moments match the evolved M1 ones, is enough to ensure convergence to the exact solution and mitigate the statistical noise that is so characteristic of the MC-based methods, among other advantages. The resulting scheme outperforms both the M1 and MC approaches, providing a comprehensive and accurate solution in both regimes.

The remainder of this work is organized as follows. In Sec. II we provide an overview of the two formalisms (M1 and MC) that are essential for constructing the GM formalism. Following that, Sec. III is dedicated to the presentation and discussion of the complete GM formalism. In Sec. IV we present several test problems designed to validate both the validity and accuracy of our formalism. Finally, we present our conclusions and describe possible improvements on the GM formalism. Additionally, in Appendix A we include the additional steps to also incorporate the neutrino number density in our formalism. Appendix B describes the tetrad transformation necessary to set the 4-momentum of the neutrinos in the MC scheme.

II. BUILDING BLOCKS: TRUNCATED MOMENTS AND MONTE CARLO

The neutrino radiation transport can be fully described by the distribution function of neutrinos $f_\nu(x^a, p^a)$ in the seven-dimensional phase space given by the spacetime coordinates $x^a = (t, x^i)$ and the neutrino 4-momentum p^a satisfying approximately the null condition $p^a p_a = 0$. This distribution function allow us to define the number of neutrinos within a six-dimensional volume of phase space,[1]

$$N(t) = \int dx^3 \frac{dp^3}{h^3} f_\nu(t, x^i, p_j). \tag{1}$$

One can also define the neutrino stress-energy tensor

$$T^{ab}(t, x^i) = \int \frac{dp^3}{h^3 \sqrt{-g} p^t} p^a p^b f_\nu(t, x^i, p_j), \tag{2}$$

[1]Notice that the momentum volume $\frac{dp^3}{h^3\sqrt{-g}p^t}$ and the spatial volume $dx^3\sqrt{-g}p^t$ are invariant under coordinate transformations, such that the six-dimensional volume in the phase space dx^3dp^3 is also invariant.

where g is the determinant of the spacetime metric g_{ab}. This radiation stress-energy tensor can also be interpreted as the energy-integrated second moment of the distribution function f_ν, as defined in [44,45].[2] In addition, in these works it was shown that any given moment includes the lower-rank ones, meaning that the (energy-integrated) zeroth and first moments can be constructed from projections of this stress-energy tensor.

The distribution function for each neutrino species[3] evolves according to the Boltzmann equation

$$p^a\left[\frac{\partial f_\nu}{\partial x^a}-\Gamma^b_{ac}p^c\frac{\partial f_\nu}{\partial p^b}\right]=\left[\frac{\partial f_\nu}{\partial \tau}\right]_{\rm coll}, \tag{3}$$

where the right-hand side includes all collisional processes (i.e., emission, absorption, and scattering) and Γ^a_{bc} are the Christoffel symbols associated with the spacetime metric g_{ab}.

Therefore, solving the Boltzmann equation requires the time evolution of a six-dimensional function, a very demanding computational challenge even with modern facilities. Here we consider two different approximations for efficiently solving the Boltzmann equation: the truncated moment formalism (M1), in which only the lowest moments of the distribution function are evolved, and direct simulation MC methods that attempt to directly solve the Boltzmann equation. We first give a short summary of these formalisms, and continue with a new method that profits from efficiently combining both of them.

In what follows we use the standard $3+1$ decomposition to write the covariant equations explicitly as an evolution system of partial differential equations. First, the spacetime metric is decomposed as

$$ds^2=-\alpha^2dt^2+\gamma_{ij}(dx^i+\beta^i dt)(dx^j+\beta^j dt), \tag{4}$$

where α is the lapse function, β^i is the shift vector, γ_{ij} is the induced 3-metric on each spatial slice, and γ is its determinant. Within this decomposition, the normal vector to the hypersurfaces is just $n_a=(-\alpha,0)$. We also use the standard definition of the extrinsic curvature K_{ij} as the Lie derivative of γ_{ij} along the normal vector n^a. Throughout this paper, from now on, we adopt the units $G=c=h=1$.

[2]Roughly speaking, the k-order moment definition includes the integral of k moments $p^{a_1}\ldots p^{a_k}$, multiplied by the weighted distribution function f_ν/ν^{k-2} and using the invariant integration volume in momentum space $\frac{dp^3}{h^3\sqrt{-g}p^t}=\nu d\nu d\Omega$, where ν is the neutrino energy. The energy-dependent moments are obtained by integrating only the solid angle $d\Omega$ on a unit sphere. When this integration also includes $d\nu$, they are called k-order energy-integrated moments ([5,44]).

[3]By "neutrino species" we refer to electron, muon, and tau neutrinos (ν_e,ν_μ,ν_τ) and their respective antineutrinos $(\bar\nu_e,\bar\nu_\mu,\bar\nu_\tau)$.

A. Truncated moment formalism: M1 approach

The truncated moment formalism evolves the lowest moments of the neutrino distribution function. In particular, the M1 scheme considers the evolution of the first two moments of the distribution function, which still depend on the neutrino energy (i.e., but not on the direction of the neutrino 4-momentum). While the moment formalism can theoretically accommodate a discretization in neutrino energies, this introduces an additional dimension that significantly escalates the required computational resources. To reduce this computational cost and avoid further technical complexities, it is common to adopt the *grey* approximation, where we primarily focus on evolving energy-integrated moments.[4] A more detailed description of the formalism and our implementation was presented in [58].

Let us define the fields that describe our evolution equations in terms of the neutrino radiation stress-energy tensor, which as mentioned before also contains the lower-order (energy-integrated) moments. The interaction between neutrinos and matter is usually simplified in the fluid rest frame. Therefore, a convenient decomposition of this tensor in terms of the spatial projection of the second and lower moments is given by

$$T^{ab}=Ju^au^b+H^au^b+H^bu^a+Q^{ab}, \tag{5}$$

where the energy density J, flux density H^a, and symmetric pressure tensor Q^{ab} of the neutrino radiation are computed by an observer comoving with the fluid. Notice that, by construction, both the flux and pressure tensors are orthogonal to the fluid velocity, i.e., $H^au_a=Q^{ab}u_b=0$.

In order to obtain a well-posed system of partial differential equations in a conservative form, it is preferable to decompose the same tensor T^{ab} in the inertial frame, namely,

$$T^{ab}=En^an^b+F^an^b+F^bn^a+P^{ab}, \tag{6}$$

where the radiation energy density E (i.e., the energy-integrated zeroth moment), radiation flux F^a (i.e., the spatial projection of the energy-integrated first moment), and symmetric radiation pressure tensor P^{ab} (i.e., the spatial projection of the energy-integrated second moment) are now evaluated by normal observers. Note that F^a and P^{ab} are orthogonal to n_a by construction, i.e., $F^an_a=0=P^{ab}n_b=0$.

We can express the fluid-rest-frame quantities $\{J,H^a,Q^{ab}\}$ in terms of the Eulerian ones $\{E,F_a,P_{ab}\}$

[4]Notice that the neutrino energy spectra is required to compute the energy-averaged opacities/emissivities. Since this energy spectra is only known exactly in the optically thick regime, an "energy" closure is necessary to complete the M1 grey approximation. The choice of such closure might have a significant impact on the electron fraction of the ejecta produced in neutron star mergers.

by decomposing the fluid 4-velocity as $u^a = W(n^a + v^a)$, where $W = -n_a u^a$ is the Lorentz factor and v^a is the spatial velocity of the fluid. (The full expressions of these frame transformations can be found, for instance, in [57,58].) As usual, the normalization of the 4-velocity $u_a u^a = -1$ allows us to explicitly compute the Lorentz factor as $W = (1 - v_i v^i)^{-1/2}$. In particular, we use the relations

$$J = W^2(E - 2F^a v_a + P^{ab} v_a v_b), \tag{7}$$

$$H^a = W(E - F^b v_b) h^a{}_c n^c + W h^a{}_b (F^b - v_c P^{bc}), \tag{8}$$

where $h_{ab} \equiv g_{ab} + u_a u_b$ is the projection tensor orthogonal to the 4-velocity of the fluid, $h_{ab} u^a = 0$. Notice that when the fluid is at rest, $v_i = 0$, the translation between frames is trivial, i.e., $E = J$, $F^a = H^a$, and $P^{ab} = Q^{ab}$.

The conservation of energy and linear momentum implies that

$$\nabla_b T^{ab} = \mathcal{S}^a, \tag{9}$$

where ∇ is the covariant derivative operator compatible with the spacetime metric g_{ab} and $\mathcal{S}^a$ is the term representing the interaction between the neutrino radiation and the fluid. This term can be written as

$$\mathcal{S}^a = (\eta - \kappa_a J) u^a - (\kappa_a + \kappa_s) H^a, \tag{10}$$

where η is the energy-averaged neutrino emissivity and (κ_a, κ_s) are the energy-averaged absorption and scattering opacities.

The conservation equation (9) in the $3+1$ decomposition ([45]) can be written as

$$\begin{aligned} &\partial_t(\sqrt{\gamma} E) + \partial_i[\sqrt{\gamma}(\alpha F^i - \beta^i E)] \\ &\quad = \alpha\sqrt{\gamma}[P^{ij} K_{ij} - F^i(\partial_i \alpha)/\alpha - \mathcal{S}^a n_a], \end{aligned} \tag{11}$$

$$\begin{aligned} &\partial_t(\sqrt{\gamma} F_i) + \partial_j[\sqrt{\gamma}(\alpha P^j{}_i - \beta^j F_i)] \\ &\quad = \sqrt{\gamma}\left[-E\partial_i \alpha + F_j \partial_i \beta^j + \frac{\alpha}{2} P^{kj} \partial_i \gamma_{kj} + \alpha \mathcal{S}^a \gamma_{ia}\right]. \end{aligned} \tag{12}$$

This system strongly resembles the hydrodynamical equations except for the fluid-neutrino interaction term $\mathcal{S}^a$, which is given in the $3+1$ decomposition by

$$\begin{aligned} \mathcal{S}_n &= -\mathcal{S}^a n_a = W[(\eta + \kappa_s J) - (\kappa_a + \kappa_s)(E - F_i v^i)], \\ \mathcal{S}_i &= \mathcal{S}^a \gamma_{ia} = W(\eta - \kappa_a J) v_i - (\kappa_a + \kappa_s) H_i. \end{aligned} \tag{13}$$

The evolution equations Eqs. (11) and (12) represent the M1 formalism. Notice that they are exact, although with two limitations: (i) there is no closed form due to the unknown second moment P^{ij} (or, conversely, Q^{ij}), and (ii) the energy-averaged emissivities/opacities $(\eta, \kappa_a, \kappa_s)$ require information about the energy spectra which is not computed explicitly within the formalism.

1. Closure relations

In general, the second moment P^{ij} depends on not only the local values of the lower moments (E, F^k) at a point, but also the global geometry of these fields in a neighborhood of that point. Although approximate closures can be defined at different limits, there is no single closure prescription $P^{ij} = P^{ij}(E, F^k)$ that accurately describes all possible regimes. Instead, the M1 scheme usually employs an analytic closure that interpolates P^{ij} between two limits: the optically thick limit (where matter and radiation are in thermodynamic equilibrium) and the optically thin limit (where the propagation of radiation, in a transparent medium, comes from a single point source). Fortunately, there are explicit expressions for P_{ij} in both limits, $\{P^{\text{thin}}_{ij}, P^{\text{thick}}_{ij}\}$, that give the following closure:

$$P^{\text{M1}}_{ij} = \frac{3\chi(\xi) - 1}{2} P^{\text{thin}}_{ij} + \frac{3[1 - \chi(\xi)]}{2} P^{\text{thick}}_{ij} = d_{\text{thin}} P^{\text{thin}}_{ij} + d_{\text{thick}} P^{\text{thick}}_{ij}, \tag{14}$$

where $\chi(\xi) \in [\frac{1}{3}, 1]$ is the variable Eddington factor and $\xi \in [0, 1]$ is the norm of the normalized flux. (For more details see [68].)

As discussed in [45], there are several relativistic generalizations for ξ, but the only one that is accurate in the optically thick limit is

$$\xi \equiv \sqrt{\frac{H_a H^a}{J^2}}. \tag{15}$$

Unfortunately, this choice is computationally expensive since the calculation of ξ requires a root-finding method to transform the fields from the inertial to the fluid rest frame. A detailed root-finding routine was used and explained in [58].

We choose the commonly employed Minerbo closure [69], which is exact in both limits,

$$\chi(\xi) = \frac{1}{3} + \xi^2 \left(\frac{6 - 2\xi + 6\xi^2}{15}\right). \tag{16}$$

However, notice that there are many other choices (see [70]) that might also accurately capture these two limits.

In the optically thick limit (or diffusion limit), the radiation pressure tensor measured by the fluid rest frame is simply described by $Q^{\text{thick}}_{ab} = J_{\text{thick}} h_{ab}/3$. To obtain the

pressure tensor $P^{\rm thick}_{ij}$ in the inertial frame, we first need to compute the intermediate quantities, $\{J_{\rm thick}, H^i_{\rm thick}, H^n_{\rm thick}\}$, that relate the fluid rest frame with the inertial frame. The final closure can be written as

$$\begin{aligned} P^{\rm thick}_{ij} &= \frac{4}{3} J_{\rm thick} W^2 v_i v_j + W(H^{\rm thick}_i v_j + H^{\rm thick}_j v_i) \\ &\quad + \frac{1}{3} J_{\rm thick} \gamma_{ij}, \\ J_{\rm thick} &= \frac{3}{2W^2+1}[(2W^2-1)E - 2W^2 F^k v_k], \\ H^i_{\rm thick} &= \frac{F^i}{W} + \frac{W v^i}{2W^2+1}[(4W^2+1)F^k v_k - 4W^2 E]. \end{aligned} \tag{17}$$

In these regions the radiation satisfies $H^a \approx 0$ (i.e., $\xi \approx 0$ and $\chi \approx 1/3$), so $P^{\rm M1}_{ij} \approx P^{\rm thick}_{ij}$.

In the optically thin limit, we assume that radiation is streaming at the speed of light in the direction of the radiation flux, leading to the explicit relation

$$P^{\rm thin}_{ij} = \frac{F_i F_j}{F^k F_k} E. \tag{18}$$

In these regions, $H^a H_a \approx J^2$ (i.e., $\xi \approx 1$ and $\chi \approx 1$), so $P^{\rm M1}_{ij} \approx P^{\rm thin}_{ij}$. Unfortunately, this limit is not unique as it is determined by the nonlocal geometry of the radiation field. In general, $P^{\rm thin}_{ij}$ will not correctly describe free-streaming neutrinos produced by multiple sources, since in vacuum they usually do not propagate in the same direction. For instance, the trajectory of colliding beams will propagate unphysically in the direction of their average momentum, as is very well represented by the well-known double-beam test (see, e.g., [46,49,56]), which will be discussed in Sec. IV B. This behavior is responsible for unphysical radiation shocks and leads, in general, to incorrect results in some scenarios. (For further details, see [5].) Dealing with these issues requires going beyond the M1 formalism. In Sec. IV B, we illustrate how both the MC scheme and our GM formalism sidestep this problem, allowing both beams to follow their original paths without interference.

B. Direct simulation Monte Carlo: MC approach

MC methods attempt to sample the distribution function $f_{(\nu)}$ with a discrete set of *neutrino packets* describing a large number of neutrinos that interact with the matter and propagate through the numerical grid. In an MC simulation, the ensemble of $N_{\rm T}$ packets at time t, each labeled by the index k and containing N_k neutrinos located at spatial coordinates x^i_k with 4-momentum p^a_k, serves as an approximation of the distribution function,[5]

$$f_\nu \sim f_{(\nu)} = \sum_{k=1}^{N_{\rm T}} N_k \delta^3(x^i - x^i_k)\delta^3(p_i - p^k_i). \tag{19}$$

Given this sampled distribution function, we can compute the radiation stress-energy tensor averaged in the neighborhood of the point x^i (i.e., for instance, a grid cell of volume $\Delta V = \Delta x^3$), namely,

$$\bar{T}^{ab}(t, x^i) = \sum_{k \in \Delta V} N_k \frac{p^a_k p^b_k}{\sqrt{-g}\Delta V p^t_k}, \tag{20}$$

where the summation only involves neutrino packets located within the volume ΔV. Notice that the MC pressure tensor just reduces to

$$P^{\rm MC}_{ij} = \bar{P}_{ij} = \sum_{k \in \Delta V} N_k \frac{p^k_i p^k_j}{\sqrt{-g}\Delta V p^t_k}. \tag{21}$$

In an MC transport scheme, the Boltzmann equation for $f_{(\nu)}$ can be translated into prescriptions for the creation, annihilation, scattering, and propagation of the neutrino packets sampling $f_{(\nu)}$. These prescriptions are explained in more detail in the following subsections.

1. Free propagation

In the absence of collisional terms, a direct substitution of the discrete distribution function (19) into the Boltzmann equation (3) implies that neutrino packets follow geodesic equations. Specifically,

$$\frac{dx^\mu}{d\lambda} = p^\mu, \qquad \frac{dp_i}{d\lambda} = \Gamma^\mu{}_{i\nu} p_\mu p^\nu, \tag{22}$$

with the normalization condition

$$p^a p_a = -m^2_\nu, \tag{23}$$

where λ is an affine parameter and m_ν is the neutrino mass. By using the $3+1$ decomposition, we rewrite these equations in the grid frame in a form suitable for time evolution,

$$\frac{dx^i}{dt} = \gamma^{ij}\frac{p_j}{p^t} - \beta^i, \tag{24}$$

$$\frac{dp_i}{dt} = -\alpha(\partial_i \alpha)p^t + (\partial_i \beta^j)p_j - \frac{1}{2p^t}(\partial_i \gamma^{jk})p_j p_k, \tag{25}$$

$$p^t = \frac{1}{\alpha}\sqrt{m^2_\nu + \gamma^{ij} p_i p_j}. \tag{26}$$

[5]It is important to highlight that using lower indices in p_i and upper indices in x^i is essential to maintain the relativistic invariance of this equation.

Since the neutrino mass is negligible compared to the energy scale of the system, it is common to assume $m_\nu = 0$, which implies that the neutrino 4-momentum p^a is null.

2. Emission

Copious amounts of neutrinos are produced in hot and dense matter. These neutrinos are emitted isotropically in the fluid frame, a process that involves the creation of new neutrino packets in the MC formalism.

For a given neutrino species, if η denotes the total emissivity (i.e., the energy of neutrinos emitted per time interval Δt and unit volume ΔV), the total energy of the emitted neutrinos is given by

$$E_{\rm ems} = \sqrt{-g}\Delta V \Delta t \eta, \tag{27}$$

where the emissivity is assumed to remain constant throughout a time step. Following [18,21,22], the number of neutrino packets emitted in the fluid frame within a given energy bin $[E_{b-1}, E_b]$ for a specific value of η_b can be approximated as

$$N_p^{(b)} \approx \frac{E_{\rm ems}}{E_{\rm packet}} \approx \sqrt{-g}\Delta V \Delta t \frac{\eta_b}{E_{\rm packet}}. \tag{28}$$

Since the total emissivity is the sum of the emissivities in each energy bin (i.e., $\eta = \sum_b \eta_b$), the total number of created packets within a cell is just $N_p = \sum_b N_p^{(b)}$. All packets are initialized with the fluid-rest-frame energy $\nu = (E_{b-1} + E_b)/2$ and represent a number of neutrinos $N_k = E_{\rm packet}/\nu$.

In practice, the procedure for packet creation can be described as follows:

(1) Compute the energy in thermal equilibrium $E_{\rm thermal}$ by using the blackbody function for the neutrino density B_ν. In many cases, we can use Kirchhoff's law $\eta = B_\nu \kappa_a$, that is,

$$E_{\rm thermal} = B_\nu \Delta V = \Delta V \frac{\eta}{\kappa_a}, \tag{29}$$

where we recall that κ_a is the absorption opacity.

(2) Compute the energy of the neutrino packet in terms of a free parameter $N_{\rm tr}$, which sets the number of packets required to describe the neutrinos in thermal equilibrium with matter, namely,

$$E_{\rm packet} = E_{\rm thermal}/N_{\rm tr}. \tag{30}$$

Notice that the choice of $N_{\rm tr}$ will influence how computational resources are distributed on our grid, i.e., to determine whether more or fewer MC packets are generated.

(3) Estimate the number of packets that should be created using the estimate (28). For a single energy bin and using Kirchhoff's law, this relation can be simplified to

$$N_p = \frac{E_{\rm ems}}{E_{\rm packet}} \approx \Delta t \kappa_a N_{\rm tr}. \tag{31}$$

Once the number of packets has been determined, their setup proceeds as follows. The packet's location is randomly drawn from a homogeneous distribution within the designated cell in the spatial coordinates of the simulation x^i. The emission time of neutrinos is randomly selected from a uniform distribution in time, and the emitted neutrinos are subsequently evolved until the end of the current time step. The new neutrino packets are emitted isotropically in the fluid rest frame, such that the neutrino 4-momentum in this frame can be initialized as

$$p_k^{a'} = \nu_k (1, \sin\theta\cos\phi, \sin\theta\sin\phi, \cos\theta). \tag{32}$$

We draw $\cos\theta$ from a uniform distribution in $[-1, 1]$ and ϕ from a uniform distribution in $[0, 2\pi]$. In order to convert the neutrino 4-momentum from the fluid rest frame to the inertial frame, we use the transformations described in Appendix B.

3. Absorption and elastic scattering

The interaction of neutrinos with matter might lead to the absorption of the neutrinos, increasing the energy of the fluid, or to a scattering where the energy is conserved but the propagation direction changes. In the MC formalism, the absorption process involves the destruction of neutrino packets, whereas scattering involves a change in the 4-momentum of the neutrinos.

To evolve a neutrino packet over a time interval Δt_p, we first determine whether the packet is free streaming or if it undergoes absorption or scattering by the fluid. The probabilities of absorption and scattering can be computed from the infinitesimal optical depth along a geodesic given by $d\tau = \kappa \nu d\lambda = (\kappa\nu/p^t)dt$, where $d\lambda$ represents the increment in the affine parameter ($p^a = dx^a/d\lambda$). The time intervals before the first absorption/scattering are then given by a Poisson distribution (see, e.g., [34]),

$$\Delta t_a = -\kappa_a^{-1} \frac{p^t}{\nu} \ln r_a, \qquad \Delta t_s = -\kappa_s^{-1} \frac{p^t}{\nu} \ln r_s, \tag{33}$$

with r_s and r_a drawn from a uniform distribution in $(\delta, 1]$, where δ is a very small number.

We then identify the smallest among the three time intervals $(\Delta t_p, \Delta t_a, \Delta t_s)$. If Δt_p is the smallest, the packet is propagated by Δt_p following the geodesic equations without interacting with the fluid. If Δt_a is the smallest, the packet is propagated by Δt_a and subsequently absorbed, leading to its removal from the simulation. Last, if Δt_s is the smallest, the packet is propagated by Δt_s and then scattered by the fluid. Following scattering events, we begin a new time step with $\Delta t_p \to \Delta t_p - \Delta t_s$.

Scattering is performed in the fluid rest frame. As we only consider isotropic elastic scattering, we simply redraw

the 4-momentum $p_k^{a'}$ (at constant fluid-rest-frame energy ν_k) from the same isotropic distribution as during the packet creation [i.e., see Eq. (32)].

III. GUIDED MOMENTS FORMALISM

Our goal is to combine the M1 and MC formalisms into a single one, capitalizing on the strengths of each while mitigating their respective weaknesses. On the one hand, the MC formalism is well known for its remarkable simplicity, since the neutrino interactions can be modeled either by solving ordinary differential equations or relying on simple stochastic processes. Moreover, the error does not scale with the dimensionality of the problem, allowing to achieve in high-dimensional problems (i.e., like the Boltzmann equation) a fairly well resolved solution with a reasonable amount of resources. However, the MC formalism also has two main drawbacks:

(1) An inherent large statistical error that decays slowly with the total number of packets, $\mathcal{O}(N_{\mathrm{T}}^{-1/2})$.
(2) A high computational cost for evolving optically thick regions, where many packets are constantly created and reabsorbed.

On the other hand, the M1 formalism (with the grey approximation) stands out for its distinct advantage in evolving equations similar to those found in hydrodynamics, which can be solved accurately with high-order finite-difference/-volume numerical methods. However, this approach comes with two significant challenges:

(1) The closure for the second moment is known exactly only in two scenarios: when neutrinos are in thermal equilibrium with the fluid in optically thick regimes, or when there is a single radiation source in the optically thin limit. Beyond these limits, the closure is merely approximated.
(2) Within the grey approximation, emissivities and opacities are averaged over neutrino energies using the Fermi-Dirac distribution function, that is, assuming neutrinos are in local thermal equilibrium with the fluid. This estimate is accurate only in optically thick regimes, but it deviates significantly from the true solution in other regimes.

One could combine the strengths of each formalism and avoid their weaknesses by solving them simultaneously. The MC formalism provides the evolution of the neutrino distribution function, which could be employed to compute the closure relation for the second moment as well as the emissivities/opacities in the M1 formalism. The M1 formalism provides an accurate solution that can be used to reduce the statistical error in the MC solution without significantly increasing the cost of the simulation. In addition, it might also solve the other main issue in MC simulations: the high cost of evolving optically thick regions. We can simply rely on the M1 formalism in optically thick regions, where it is very accurate, and evolve more MC packets only below a certain optical depth. Finally, and most importantly, as the MC evolution asymptotes to the exact solution of the Boltzmann equation, and since the M1 evolution can take information[6] from MC solutions, the algorithm for M1 converges to a true solution of the Boltzmann equation for an infinite spatial grid resolution and infinite number of neutrino packets.

Actually, the combination of M1 and MC formalisms was already attempted in [18], where all of these issues were discussed in detail. However, it was also stated that it was not clear if the coupled MC-M1 system was numerically stable, and whether any additional work might be required to guarantee that the coupled MC-M1 equations are well behaved for realistic astrophysical simulations. We believe that the MC-M1 problems that were observed in that work were due to an imbalance in the information flow. The M1 equations received information from the MC solution (i.e., by using the discrete distribution function) to compute the closure relation and the energy-averaged emissivities/opacities within the grey approximation. However, there was no feedback from the M1 solutions into the MC equations, not even in the optically thick regions where the former solutions should be fairly accurate. Therefore, it seems natural to think that the missing crucial step consists of passing this information from the M1 solutions to the MC distribution function.

Inspired by the moment-guided MC approach ([66,67]), an advanced numerical method from applied mathematics to combine the kinetic and Euler equations, we have designed a way to project the MC distribution function such that its lowest moments match exactly to the ones evolved by the M1 equations. Our GM formalism shares some features with the original method, although the application to the relativistic neutrino transport problem also presents many differences. The remainder of this section is devoted to describing the basics of our method and explaining how it can be applied specifically for this particular problem of neutrino transport.

A. Basics of the method

Our goal is to solve the Boltzmann equation with an MC formalism and the truncated moments formalism simultaneously by using any type of finite-difference or finite-volume scheme. We assume that an *exact* second moment P_{ij} can be written as the pressure tensor calculated with the M1 closure relation P_{ij}^{M1} plus a correction term that can only be evaluated by using the distribution function of the neutrinos. By including this correction, both the M1 and MC formalisms should provide the same results in terms of macroscopic quantities (i.e., the lowest moments), except for numerical errors. It is natural to assume that the set of

[6]In this context, we mean all of the missing information about higher moments and the neutrino energy spectra, which would otherwise be approximated using analytical prescriptions.

moments $\mathcal{J}_a$ obtained from the truncated moments formalism represents in general a better statistical estimate than the moments $\bar{\mathcal{J}}_a$ calculated from the MC method [they will be defined explicitly in Eqs. (37) and (38) below], since the resolution of the truncated moment equations does not involve any stochastic process.

Let us assume that at time t^n the lowest moments constructed with the sampled MC distribution function $f^n_{(\nu)}$ are consistent with those evolved by the M1 formalism (i.e., $\bar{\mathcal{J}}^n_a = \mathcal{J}^n_a$). Thus, we can summarize the method to evolve the solution from t^n to t^{n+1} in the following way:

(1) Solve the Boltzmann equation with an MC scheme to obtain an approximated solution $f^*_{(\nu)}$ at t^{n+1}, which is used for calculating the first set of moments $\bar{\mathcal{J}}^*_a$.
(2) Solve the M1 equations with a finite-volume/-difference scheme, using the distribution function $f^n_{(\nu)}$ to calculate the correction term appearing in the closure for the exact second moment. The evolved M1 fields allow to reconstruct the second set of moments $\mathcal{J}^{n+1}_a$ at t^{n+1}.
(3) Match the lowest MC moments to the lowest M1 ones through a transformation T of the sample values, $f^{n+1}_{(\nu)} = T(f^*_{(\nu)})$, such that $\bar{\mathcal{J}}^{n+1}_a = \mathcal{J}^{n+1}_a$.
(4) Restart the computation at the next time step.

The piece that was missing in previous works was Step 3. We will focus on that transformation after giving some details on the application of this abstract scheme to the specifics of the neutrino transport problem.

B. Guided moments for neutrino transport

The first step of the GM formalism consists of just performing a standard evolution using the MC method, which can also be applied directly to our problem. At the second step, the M1 equations are evolved by using the exact P_{ij}, which necessarily must include corrections from the sampled distribution function. There is not a unique way to incorporate these corrections, leading to several possible choices. The exact closure that is more similar to the one presented in the original work [66,67] would be

$$P_{ij} = P^{\rm thick}_{ij} + \int \frac{dp^3}{h^3\sqrt{-g}p^t} p_i p_j (f_\nu - f^{\rm eq}_\nu), \quad (34)$$

where $f^{\rm eq}_\nu$ is the Fermi-Dirac distribution function for neutrinos in thermodynamic equilibrium with the fluid. Note that to obtain this exact closure we have used

$$P^{\rm thick}_{ij} = \int \frac{dp^3}{h^3\sqrt{-g}p^t} p_i p_j f^{\rm eq}_\nu, \quad (35)$$

although for the evolution one would use the expression given by Eq. (17). Therefore, one would solve $P^{\rm thick}_{ij}$ using either a finite difference or finite volume scheme and the deviations from the equilibrium state with the sampled distribution function. Another exact closure might be obtained by using information only from the MC formalism, that is, $P_{ij} = P^{\rm MC}_{ij}$. However, this choice would not mitigate the issues related to the MC scheme.

Although in realistic applications one of the previous options might be more suitable, for simplicity we chose a final pressure tensor $P^{\rm GM}_{ij}$ given by the following straightforward combination[7]:

$$P^{\rm GM}_{ij} = h(\xi)P^{\rm MC}_{ij} + [1 - h(\xi)]P^{\rm M1}_{ij}, \quad (36)$$

where $h(\xi)$ is a smooth function of the normalized flux that vanishes in the optically thick limit [i.e., $h(\xi \to 0) = 0$] and goes to unity in optically thin media [i.e., $h(\xi \to 1) = 1$]. This splitting allows us to not only accurately recover the optically thick regime with the M1 formalism, but also introduce corrections by using the MC distribution function as the neutrinos move away from that regime.

The third step of our method involves the matching of moments. It is useful to define them as a four-dimensional covector $\mathcal{J}_a$ (i.e., equivalent to the first moment; see, [44,45]), constructed by projecting the stress-energy tensor with the normal to the hypersurfaces, that is,

$$\mathcal{J}^{\rm M1}_a = \mathcal{J}_a \equiv -T_{ab}n^b = En_a + F_a. \quad (37)$$

Clearly, this is a convenient way to deal with the zeroth and (projected) first moment (E, F_i) within a four-dimensional moment. We denote this quantity as $\mathcal{J}^{\rm M1}_a$ when it is calculated using the evolved moments from the M1 formalism.

We want to match these moments with the equivalent quantities $\bar{\mathcal{J}}_a$ computed from the MC discrete distribution, namely,

$$\mathcal{J}^{\rm MC}_a = \bar{\mathcal{J}}_a \equiv -\bar{T}_{ab}n^b = \sum_{k\in\Delta V} N_k \frac{p^k_a}{\sqrt{\gamma}\Delta V}. \quad (38)$$

Using the expression for null neutrino momentum $p^k_a = \epsilon_k(n_a + l^k_a)$, with $n^a l^k_a = 0$, the MC moments can be written as

$$\bar{\mathcal{J}}_a = \sum_{k\in\Delta V} \frac{N_k\epsilon_k}{\sqrt{\gamma}\Delta V}(n_a + l^k_a), \quad (39)$$

where $\epsilon_k = -p^k_a n^a$ is just the neutrino energy measured in the inertial frame. If we project $\bar{\mathcal{J}}_a$ along and perpendicular to the normal n_a, we find that

[7]Following [18], we reduce the statistical error in the MC pressure tensor by modifying it as $P^{\rm MC}_{ij} \to (P^{\rm MC}_{ij}/\bar{E})E$.

$$\bar{E} = \sum_{k\in\Delta V} \frac{N_k \epsilon_k}{\sqrt{\gamma}\Delta V}, \qquad \bar{F}_a = \sum_{k\in\Delta V} \frac{N_k \epsilon_k l_a^k}{\sqrt{\gamma}\Delta V}, \tag{40}$$

such that the relation $\bar{\mathcal{J}}_a = \bar{E} n_a + \bar{F}_a$ is recovered, equivalent to that of the M1 moments.

We are interested in transforming the neutrino 4-momentum p_k^a into another 4-momentum $\tilde{p}_k^a = \Lambda_b^a p_k^b$ such that

$$\mathcal{J}_a^{\mathrm{M1}} = \sum_{k\in\Delta V} N_k \frac{\tilde{p}_a^k}{\sqrt{\gamma}\Delta V}. \tag{41}$$

We can modify p_k^a to $\tilde{p}_k^a$ without changing its norm by using a Lorentz boost transformation that converts $\mathcal{J}_a^{\mathrm{MC}}$ into $\mathcal{J}_a^{\mathrm{M1}}$. Although this would correspond directly to the original moment-guided approach, we find in our tests that a better option is to choose as a target a combination of the M1 and MC moments, namely,

$$\mathcal{J}_a^{\mathrm{GM}} = h(\xi)\mathcal{J}_a^{\mathrm{MC}} + [1 - h(\xi)]\mathcal{J}_a^{\mathrm{M1}}. \tag{42}$$

The motivation for this choice is to exactly recover the M1 moments in the optically thick limit, while the MC moment remains unchanged in the optically thin limit, providing a better physical model in this regime. An explicit expression for this Lorentz transformation, which sends $\mathcal{J}_a^{\mathrm{MC}} \to \mathcal{J}_a^{\mathrm{GM}}$, is given in Sec. III C.

At this point, it is interesting to discuss the different limits of the GM formalism, which strongly depends on the profile of the function $h(\xi)$. A suitable choice could be the logistic function (see Fig. 1), a smooth approximation to the step function with two parameters to set the location of the transition ξ_0 and its steepness k, that is,

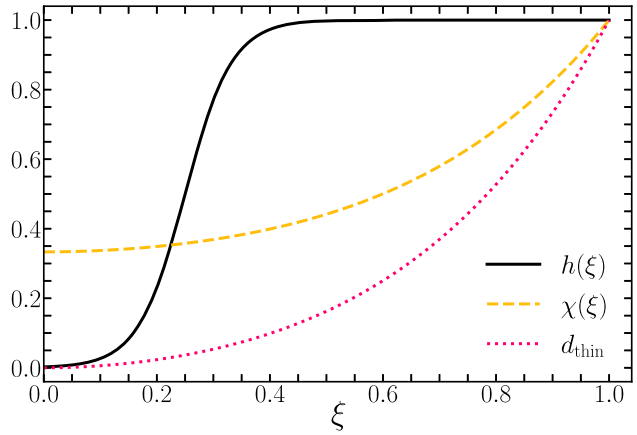

FIG. 1. Comparison between $h(\xi)$, $\chi(\xi)$ (Minerbo closure), and d_{thin}. The logistic function has the following parameter set in our tests: a transition at $\xi_0 = 1/3$ with a steepness $k = 12$, such that the optically thick regime is fully recovered for $\xi \leq 0.1$, whereas for $\xi \geq 0.5$ the MC pressure tensor fully dominates the solution.

$$h(\xi) = \frac{1}{1 + e^{-2k(\xi-\xi_0)}}. \tag{43}$$

When $\xi \to 0$, the pressure tensor is dominated by that in the optically thick limit (i.e., $P_{ij}^{\mathrm{GM}} \to P_{ij}^{\mathrm{M1}} \to P_{ij}^{\mathrm{thick}}$), while the projection (explicitly defined in the next subsection) brings the moments of the MC to match exactly the ones of the M1 (i.e., $\mathcal{J}_a^{\mathrm{MC}} \to \mathcal{J}_a^{\mathrm{GM}}$ and $\mathcal{J}_a^{\mathrm{GM}} \to \mathcal{J}_a^{\mathrm{M1}}$). In the opposite limit $\xi \to 1$, the pressure tensor is dominated by the MC one (i.e., $P_{ij}^{\mathrm{GM}} \to P_{ij}^{\mathrm{MC}}$) since in optically thin regimes the M1 solution is only valid for isolated distant sources. In this limit, only the MC solution converges to the exact solution. This is consistent with the projection on the moments, reducing to just the identity in this limit (i.e., $\mathcal{J}_a^{\mathrm{MC}} \to \mathcal{J}_a^{\mathrm{GM}}$ and $\mathcal{J}_a^{\mathrm{GM}} \to \mathcal{J}_a^{\mathrm{MC}}$).

C. Matching the moments: Lorentz boost link

We can modify p_k^a to $\tilde{p}_k^a$ without changing its norm by using a Lorentz boost transformation that sends $\bar{\mathcal{J}}_a = \mathcal{J}_a^{\mathrm{MC}}$ into $\mathcal{J}_a = \mathcal{J}_a^{\mathrm{GM}}$. Since Lorentz transformations (defined as $\Lambda_b^a g^{bc} \Lambda_c^d = g^{ad}$) preserve vector norms, and $\mathcal{J}_a^{\mathrm{MC}}$ is in general timelike and future directed, for the desired transformation to exist, $\mathcal{J}_a^{\mathrm{GM}}$ has to be timelike and future directed as well. The explanation about why these vectors satisfy such properties can be found at the end of this subsection.

The Lorentz transformations connecting a given initial vector to a final one are referred to as *Lorentz boost links*. Several transformations addressing this problem can be found in the literature (see, for example, [71,72]). We chose the simplest option that fits our scheme, that is,

$$\Lambda_b^a = \delta_b^a - \delta\Lambda_b^a,$$

where

$$\delta\Lambda_b^a = \frac{1}{-1 + \frac{\bar{\mathcal{J}}_d \mathcal{J}^d}{\mathcal{J}\bar{\mathcal{J}}}} \left(\frac{\bar{\mathcal{J}}^a}{\bar{\mathcal{J}}} + \frac{\mathcal{J}^a}{\mathcal{J}}\right)\left(\frac{\bar{\mathcal{J}}^b}{\bar{\mathcal{J}}} + \frac{\mathcal{J}^b}{\mathcal{J}}\right) + \frac{2\mathcal{J}^a \bar{\mathcal{J}}_b}{\mathcal{J}\bar{\mathcal{J}}},$$

where $\mathcal{J} = \sqrt{-\mathcal{J}_d \mathcal{J}^d}$ and $\bar{\mathcal{J}} = \sqrt{-\bar{\mathcal{J}}_d \bar{\mathcal{J}}^d}$ are the norms of the respective moments.

We notice that this transformation is always well defined since, as we mentioned before, $\bar{\mathcal{J}}_d$ and $\mathcal{J}_d$ are timelike and future directed. Therefore, $-1 \leq \frac{\bar{\mathcal{J}}_d \mathcal{J}^d}{\mathcal{J}\bar{\mathcal{J}}} < 0$, indicating that the denominators in the definition of $\delta\Lambda_b^a$ never go to zero.

This Lorentz boost link connects the two 4-vectors as follows:

$$\frac{\bar{\mathcal{J}}^a}{\bar{\mathcal{J}}} \Lambda_a^b = \frac{\mathcal{J}^b}{\mathcal{J}}. \tag{44}$$

We notice that substituting Eq. (38) into this last expression gives

$$\mathcal{J}^b = \sum_{k\in\Delta V} \frac{N_k}{\sqrt{\gamma}\Delta V}\left(\frac{\mathcal{J}}{\bar{\mathcal{J}}} p_k{}^a \Lambda_a^b\right), \tag{45}$$

which leads to the desired result

$$\mathcal{J}^b = \sum_{k\in\Delta V} N_k \frac{\tilde{p}_b^k}{\sqrt{\gamma}\Delta V} \quad \text{with} \quad \tilde{p}_b^k \equiv \frac{\mathcal{J}}{\bar{\mathcal{J}}} p_k{}^a \Lambda_a^b. \tag{46}$$

The neutrino 4-momentum $\tilde{p}_b^k$ remains timelike (or null when $m_\nu = 0$) due to the fact that the Lorentz transformation Λ_b^a preserves the norm of p_a^k. In simpler terms, we have applied a boost/rotation to the neutrino 4-momentum of all of the packets within a given cell, ensuring that the MC moments $(\bar{E}, \bar{F}_i)$ precisely match the corresponding GM moments in that specific cell.

Returning to the discussion of the norms of $\mathcal{J}_a^{\rm MC}$ and $\mathcal{J}_a^{\rm GM}$, let us assume a tiny nonzero neutrino mass $m_\nu = \delta$, although it is negligible compared with the other scales in the problem. As indicated by Eq. (38), the direct consequence is that the 4-moment $\mathcal{J}_a^{\rm MC}$ constitutes then a positive linear combination of future-directed timelike vectors. Consequently, $\mathcal{J}_a^{\rm MC}$ must also be timelike and future directed. To ensure the timelike and future-directed nature of $\mathcal{J}_a^{\rm M1}$, we impose a consistency condition $F_i F^i \leq (1-\delta)E^2$ (see [73]). Finally, considering that $\mathcal{J}_a^{\rm GM}$ [see Eq. (42)] is a positive linear combination of $\mathcal{J}_a^{\rm M1}$ and $\mathcal{J}_a^{\rm MC}$, we can conclude that it is also timelike and future directed.

IV. NUMERICAL TESTS

In this section we perform several stringent tests to validate our method and assess its accuracy. The numerical scheme employed for solving the M1 formalism was presented in detail in [58]. In summary, the evolution equations are evolved in time by using an IMEX time integrator, fourth-order accurate for the explicit part and second order for the stiff terms. The spatial discretization is based on a high-resolution shock capturing (HRSC) scheme with finite-volume reconstruction, designed to be asymptotically preserving in the diffusion equation limit [57]. The numerical scheme employed to solve the MC formalism has been elaborated upon throughout the manuscript, and it is predominantly inspired by the ones presented in [18,21,22].

In the following we present the results of four distinct numerical solutions: M1 represents the uncoupled (i.e., standalone) truncated moment approach, MC denotes the uncoupled MC method, GM1 represents M1 solutions using the GM formalism, and GMC designates MC solutions using the GM formalism. These four relevant solutions are subjected to thorough comparative analysis in the following numerical tests.

A. Diffusion in a moving medium test

Diffusion in a moving medium is a challenging test (considered also in [57–60]) that encapsulates most of the essential elements of the M1 implementation. The test consists of a pulse of radiation energy density, characterized by a Gaussian profile, propagating within a moving medium that is dominated by scattering dynamics (i.e., a high value of the scattering opacity κ_s). The complete dynamics can be accurately captured only with the correct treatment of stiff source terms.

The initial conditions at $t = 0$ are specified as follows: $E(\mathbf{x}) = e^{-9x^2}$, $v^x(\mathbf{x}) = 0.5$, $\kappa_s(\mathbf{x}) = 10^3$, and $\kappa_a(\mathbf{x}) = \eta(\mathbf{x}) = 0$. The radiation fluxes F_i are initialized under the assumption that the radiation is fully trapped (i.e., $H^a = 0$). Using the relations between frames, this condition translates into

$$J = \frac{3E}{4W^2 - 1}, \qquad F_i = \frac{4}{3} J W^2 v_i. \tag{47}$$

In order to check the convergence of the numerical solutions, we consider three different spatial resolutions, corresponding to $\Delta x = (0.01, 0.02, 0.04)$. For the evolution of the distribution function, we consider different fixed total numbers of packets $N_{\rm T} = (0.5, 1, 2, 4) \times 10^4$.

Figure 2 illustrates the radiation energy density profile at time $t = 4$, reconstructed from the MC solution, for various total numbers of packets $N_{\rm T} = (1, 2, 4) \times 10^4$. The semianalytic solution is also plotted for comparison purposes. A large number of packets has been employed to demonstrate that, as expected, with "infinite" resolution (i.e., $N_{\rm T} \to \infty$), the MC formalism converges to the true solution. However, the number of packets required for an accurate MC solution

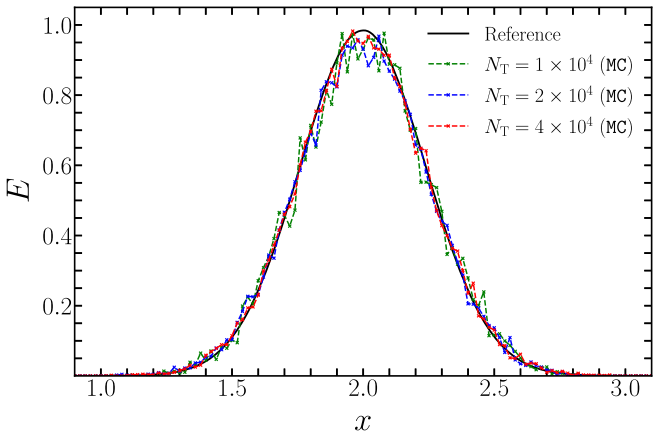

FIG. 2. Diffusion in a moving medium test. The profile of the energy density, reconstructed from the MC numerical solution, is displayed at time $t = 4$ for different total numbers of packets $N_{\rm T}$ by keeping the spatial resolution $\Delta x = 0.02$ fixed. As $N_{\rm T}$ increases, the numerical solution tends to the semianalytic (reference) one.

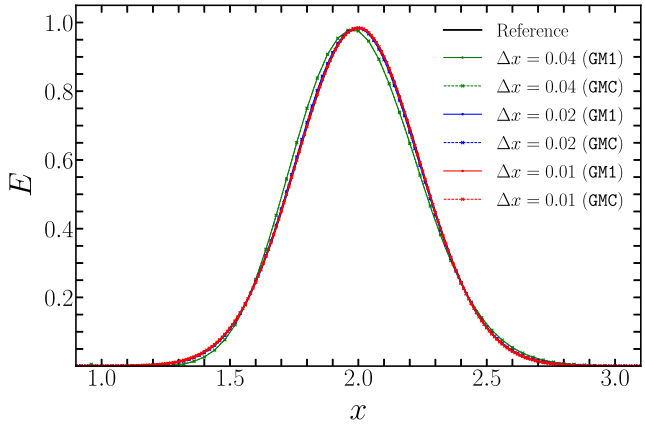

FIG. 3. Diffusion in a moving medium test. Comparison between the numerical solutions of GM1 and GMC and the semianalytic solution for several grid resolutions Δx with a number of packets $N_{\mathrm{T}} = 2 \times 10^4$ fixed. As Δx decreases, the numerical solution tends to the semianalytic (reference) one.

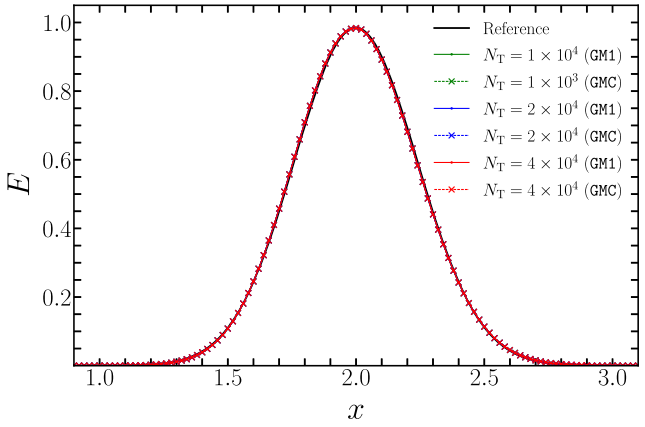

FIG. 4. Diffusion in a moving medium test. Comparison between the numerical solutions of GM1 and GMC and the semianalytic solution for various values of the total number of packets N_{T} with a grid resolution $\Delta x = 0.02$ fixed. The observed perfect matching shows that the GM solutions do not depend on the total number of packets in optically thick regimes.

in high-scattering regions is unfeasible in realistic scenarios of neutron star mergers.

This limitation is addressed by the GM scheme. In Fig. 3, the numerical solutions of GM1 and GMC are plotted for different spatial resolutions $\Delta x = (0.01, 0.02, 0.04)$, keeping $N_{\mathrm{T}} = 2 \times 10^4$ fixed. As the entire domain of this test is optically thick, we expect an almost exact matching of the lowest moments from M1 to MC with our choice of the function $h(\xi)$ [see Eq. (43) and Fig. 1]. Consequently, GM1 and GMC are anticipated to precisely follow the M1 behavior. (For a comparison between the M1 solution and the semianalytic solution, we refer to [58].) Indeed, as shown in Fig. 3, both GM1 and GMC perfectly match the M1 solution, approaching the semianalytic one as the resolution increases. It is worth noting that, in such optically thick regimes, the MC method tends to be computationally slow and usually provides a poor solution. Therefore, by choosing $h(\xi)$ as specified, we can ensure that our GM method remains as accurate and efficient as M1 in this regime.

These results are confirmed in Fig. 4, where the radiation energy density of the two GM numerical solutions is displayed by varying the total number of packets $N_{\mathrm{T}} = (1, 2, 4) \times 10^4$ but keeping the spatial resolution $\Delta x = 0.02$ fixed. As anticipated, both GM solutions remain unchanged, overlapping almost exactly with the semianalytical one. Consequently, within the GM scheme, increasing the number of packets is not necessary to enhance the numerical solution in optically thick regions.

A more quantitative analysis of the observed results can be obtained by performing suitable convergence tests of the error, which can be defined as the (norm of the) difference between the numerical and semianalytical solutions. Two types of convergence can be examined: varying the total numbers of packets while keeping the grid resolution fixed, or varying the grid resolution while keeping the total number of packets fixed. The latter is represented in Fig. 5 for a fixed number of total packets $N_{\mathrm{T}} = 2 \times 10^4$. In this case, we find the expected second order of convergence of the M1 scheme, as reported in [58]. As mentioned earlier, both the GM1 and GMC solutions closely follow the M1 solution. There exists a very small difference in the error between GM1 and GMC, originated by a few cells that contain no packets and where the matching of the moments could not be performed. The convergence for a fixed grid resolution $\Delta x = 0.02$ is displayed in Fig. 6. Here, we find the anticipated MC convergence of $N_{\mathrm{T}}^{-1/2}$. However, the errors for both GM1 and GMC are much smaller and exhibit no improvement when increasing the total number of packets. This lack of improvement is attributed to the accuracy dominance of M1 over MC in the numerical solution for this test.

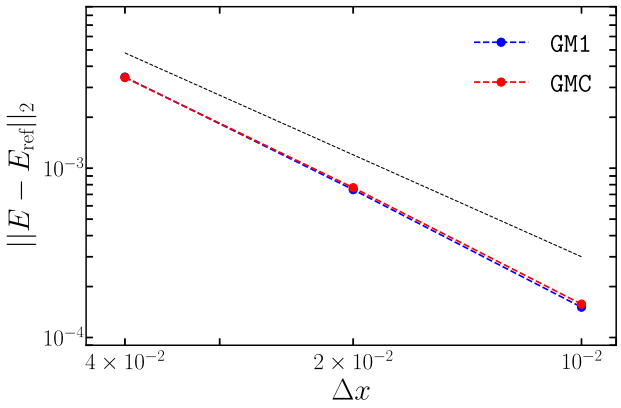

FIG. 5. Diffusion in a moving medium test. Convergence of the GM1 and GMC solutions to the reference solution for a fixed number of total packets $N_{\mathrm{T}} = 2 \times 10^4$ by varying the grid resolution. We find an approximate second-order convergence (dashed black line) for both the GM1 and GMC solutions.

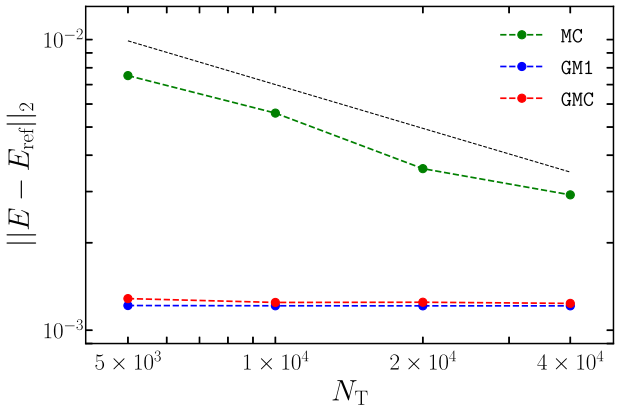

FIG. 6. Diffusion in a moving medium test. Convergence of the GM1 and GMC solutions to the reference solution for a fixed grid resolution $\Delta x = 0.02$ by varying the number of total packets. We find the expected $N_{\rm T}^{-1/2}$ convergence for the MC solution (dashed black line), but no dependence on $N_{\rm T}$ for either the GM1 or GMC solution.

B. Double beam test

This benchmark highlights the spectacular failure of the M1 formalism in optically thin regions when multiple sources are present (see, e.g., [47,49,56]). In this two-dimensional test, two radiation beams are injected into the domain. If we consider the radiation to be neutrinos, one would expect the beams to follow straight paths, crossing without interaction. However, the M1 scheme, treating radiation as a fluid, encounters challenges in this scenario since the closure is local and can only capture the physical behavior for a single source. On the other hand, the MC approach has no difficulties to find the correct physical solution.

In particular, we set the following initial conditions. We inject two beams of neutrinos from the left boundaries of the domain $(x, y) \in [-2, 2] \times [-4.5, 4.5]$ with an angle of 60° between them. In this test, we consider only a relatively high-resolution case, with a fixed spatial grid resolution $\Delta x = 0.01$ and total number of packets $N_{\rm T} = 5 \times 10^6$. The simulation is performed with the four schemes (M1, MC, GMC, GM1) until the final time $t = 0.5$, capturing the moment at which the beams have already intersected and continue along their trajectory.

The solutions of the energy density at this final time are presented in Fig. 7. As already mentioned, when two (or more) beams are present, the closure for the second moment in the M1 formalism lacks sufficient information, causing the two beams to merge into a single one propagating along the average of the original directions. Notice that, although the distribution function contains all of the information about possible directions of propagation, the M1 formalism retains only a single averaged direction: momenta in opposite directions cancel each other out, resulting in a loss of information regarding the original momentum distribution [56]. In principle, the lost information could potentially be recovered by employing higher moments. In clear contrast, in the MC scheme the two beams intersect seamlessly without losing energy density or modifying their trajectories. A similar outcome, though not as pristine, is observed for the GMC and GM1 numerical solutions. This outcome highlights a significant advantage of our GM formalism, which demonstrates an accurate handling of the solution in optically thin regions.

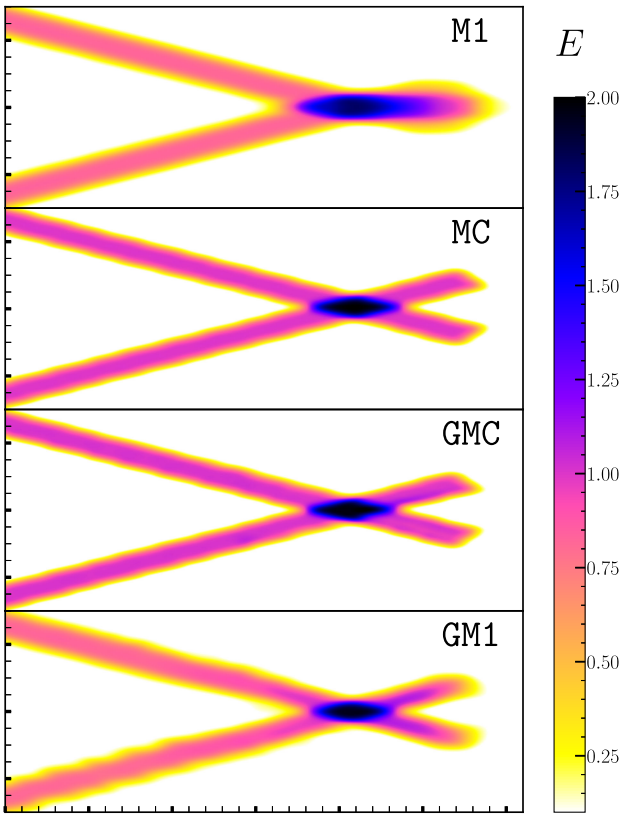

FIG. 7. Double beam test. Numerical solutions for the M1, MC, GMC, and GM1 schemes are presented at the final time $t = 0.5$, using $\Delta x = 0.01$ and $N_{\rm T} = 5 \times 10^6$ fixed. The behavior of M1 reveals a breakdown in the optically thin limit when multiple sources are present. In contrast, the MC, GMC, and GM1 solutions preserve the initial directions of the beams, enabling them to cross without interacting.

C. Radiating and absorbing sphere test

A more challenging problem, which includes both the optically thick and thin regimes, is given by a homogeneous radiating and absorbing sphere. This test, whose analytical solution is known, has been widely discussed in astrophysical literature (see, e.g., [56–60,74–79]) since it can be interpreted as a highly simplified model for an isolated, radiating neutron star.

The main configuration involves a static [i.e., $v^i(\mathbf{x}) = 0$], spherically symmetric, homogeneous sphere of radius R with a constant energy density. In this idealized

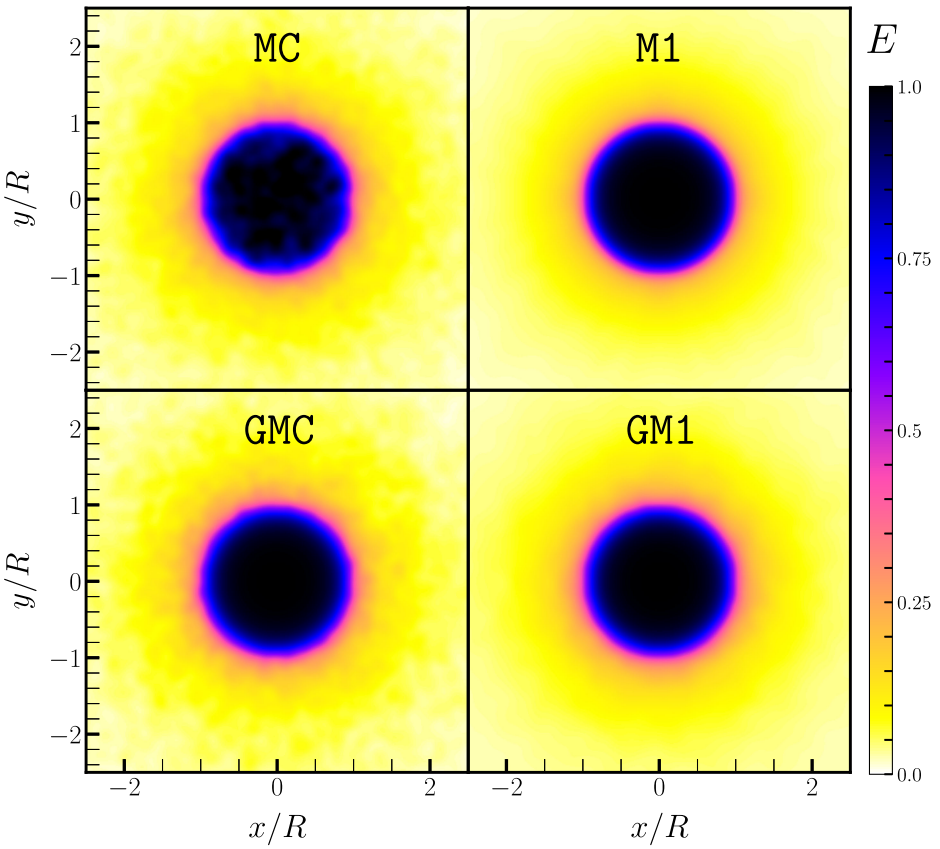

FIG. 8. Radiating and absorbing sphere test. The energy density, computed with the MC, M1, GMC, and GM1 schemes using $\Delta x = 0.03$ and $N_{\rm tr} = 80$, is displayed at the equatorial plane at time $t = 5$, when the solution has reached a steady state.

case, the only neutrino-matter interaction process allowed is the isotropic thermal absorption and emission,

$$\kappa_a(\mathbf{x},\mathbf{y},\mathbf{z}) = \eta(\mathbf{x},\mathbf{y},\mathbf{z}) = \begin{cases} 10 & \text{for } r \le R, \\ 0 & \text{for } r > R, \end{cases}$$
$$\kappa_s(\mathbf{x},\mathbf{y},\mathbf{z}) = \mathbf{0}, \tag{48}$$

where $r = \sqrt{x^2 + y^2 + z^2}$ and we have chosen $R = 0.5$. Our three-dimensional computational Cartesian domain is a cube of dimensions $[-2, 2]^3$, discretized with different spatial grid resolution resolutions $\Delta x = (0.03, 0.06, 0.12)$. In this specific scenario, characterized by a nonzero emissivity, the simulation cost of the MC scheme is governed by the free parameter $N_{\rm tr}$, related to the neutrino packets generated in a grid cell [see Eq. (30)]. In this test, we explore various values of $N_{\rm tr} = (20, 40, 80)$.

Figure 8 displays the radiation energy density in the equatorial plane of the four considered schemes (MC, M1, GMC, GM1) at time $t = 5$, when the solution has reached a steady state. These results, obtained using $\Delta x = 0.03$ and $N_{\rm tr} = 80$, are consistent with our theoretical expectations. All methods produce qualitatively similar solutions, with MC and GMC showing oscillations throughout the domain due to statistical noise (i.e., which would diminish with a greater number of packets), while M1 and GM1 exhibit much smoother profiles. In particular, GMC effectively accurately resolves the interior of the sphere, where we observe a full matching from the M1 solution onto the MC one, as expected in optically thick regions. In the exterior of the sphere, some oscillations appear due to the stochastic nature of the MC method, which is dominant in the optically thin region. The GM1 solution matches M1 in the interior of the sphere, and it smoother than GMC in the exterior. This positive outcome confirms that the GM approach retains the advantages of evolving a truncated moment scheme while incorporating new features that allow to also accurately handle the optically thin limit.

In order to quantitatively assess the accuracy of our methods, the radial profile of the energy density is compared with the analytical (reference) solution. The MC solution is presented in Fig. 9 for various numbers of packets corresponding to $N_{\rm tr} = (20, 40, 80)$, while keeping the spatial resolution $\Delta x = 0.03$ fixed. The inherent statistical noise of the MC is evident for all points in the domain, yet the solution progressively converges to the analytic one as the number of packets is increased. This test highlights one of the limitations of the MC scheme, namely, its lower convergence rate. On the other hand, the solution of the M1 formalism displays a second-order convergence

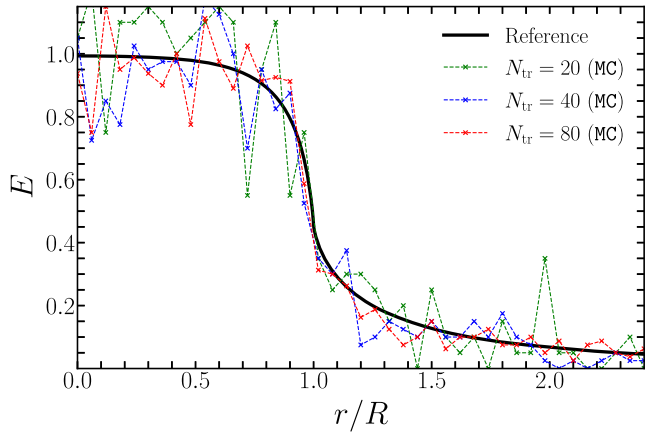

FIG. 9. Radiating and absorbing sphere test. Comparison between the MC numerical and exact solutions for various values of the number of packets $N_{\rm tr}$ with a fixed spatial resolution $\Delta x = 0.03$. The statistical noise of the numerical solution decreases as the number of packets increases.

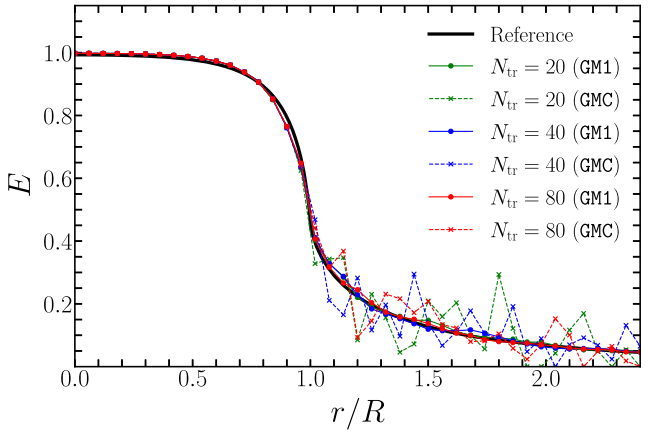

FIG. 11. Radiating and absorbing sphere test. Comparison between the numerical solutions of GM1 and GMC and the analytic one for various values of the number of packets while keeping a fixed grid resolution $\Delta x = 0.03$. As in Fig. 9, the statistical noise decreases for both numerical solutions as the number of packets increases.

when appropriate numerical schemes are employed (we refer to [58] for details).

We now turn to the results of our GM formalism. In Fig. 10, we compare the numerical solutions of GM1 and GMC with the analytic solution for different spatial resolutions $\Delta x = (0.03, 0.06, 0.12)$, while keeping the number of total packets approximately constant, setting $N_{\rm tr} = 40$. Given the optically thick regime found in the star's interior, the GMC solution exhibits no statistical noise in this region, unlike the outer region where oscillations are present. Interestingly, these oscillations are mostly suppressed in the GM1 solution. The average nature of the truncated moments formalism and the HRSC schemes employed for the evolution of the moments are probably the cause of this suppression. Finally, notice that the GM1 solution converges to the analytical one as the grid spacing decreases. However, the GMC solution only converges clearly in the interior of the sphere. Outside, there remains a statistical noise that does not depend on the grid resolution. In Fig. 11, we compare the numerical solutions of GM1 and GMC with the analytic solution for different choices of the number of packets $N_{\rm tr} = (20, 40, 80)$ keeping the spatial resolution $\Delta x = 0.03$ fixed. As expected, the statistical noise outside the sphere decreases as the number of packets increases.

Convergence tests are performed by varying the number of total packets while keeping the spatial resolution fixed and vice versa. The results of the former analysis are presented in Fig. 12, where the error in the numerical

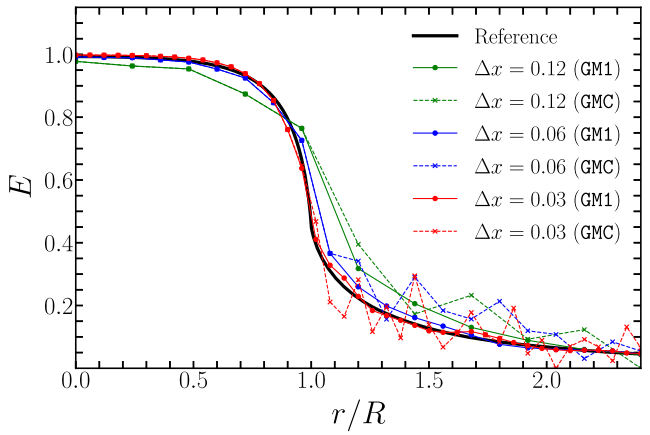

FIG. 10. Radiating and absorbing sphere test. Comparison between the numerical solutions of GM1 and GMC and the analytic solution for various grid resolutions with a fixed number of packets $N_{\rm tr} = 40$. The GM1 clearly converges to the exact solution. However, in the case of GMC, while there is clearly convergence in the interior of the star, the presence of statistical noise remains fairly consistent over all grid resolutions.

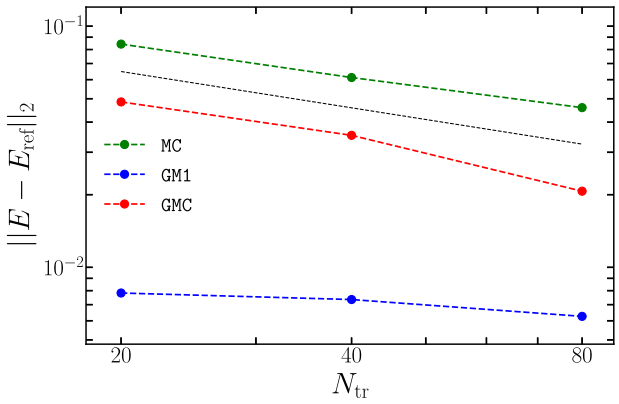

FIG. 12. Radiating and absorbing sphere test. Convergence of the MC, GM1, and GMC solutions for a fixed grid resolution $\Delta x = 0.03$ by varying the number of packets. We find the expected $N_{\rm T}^{-1/2}$ convergence (dashed black line) of the MC method except for the GM1 solution, which already presents a very small error.

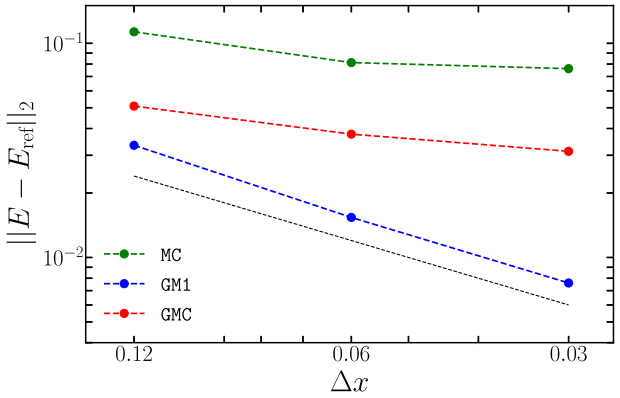

FIG. 13. Radiating and absorbing sphere test. Convergence of the MC, GM1, and GMC solutions for a fixed number of packets $N_{\rm tr} = 40$ while varying the grid resolutions. We find an approximate first-order convergence (dashed black line) for GM1 but only a moderate improvement for the MC or GMC solutions, which only converge as the number of packets increases.

solution is displayed as a function of the total number of packets for a fixed spatial resolution $\Delta x = 0.03$. Notably, the GM1 solution exhibits minimal improvement with increasing number of packets, given the dominance of the M1 solution in the interior, which already has negligible error, and the smoothness of the solution in the exterior. On the other hand, both GMC and MC demonstrate an approximate $1/2$ convergence, attributed to the suppression of statistical noise in the exterior of the star as the total number of packets increases. The convergence of the solutions as a function of the spatial grid resolution while keeping a fixed number of packets $N_{\rm tr} = 40$ is displayed in Fig. 13. Here, the GM1 solution shows a first-order convergence, while the MC and GMC solutions display only marginal improvement. This moderate improvement is mainly due to the projection of the M1 solution inside the star, while the solution in the exterior is still dominated by statistical noise which only decreases by increasing the number of packets. This result confirms that the GM formalism only converges to the exact solution for an infinite grid resolution and infinite number of packets.

D. Radiating and absorbing torus test

In our last three-dimensional problem we simulate a scenario reminiscent of the one discussed in Sec. IV B, but without so many symmetries. The astrophysical motivation behind this configuration is to reproduce a simple model of the remnant resulting from a neutron star merger. Instead of an absorbing and radiating sphere, the geometry of

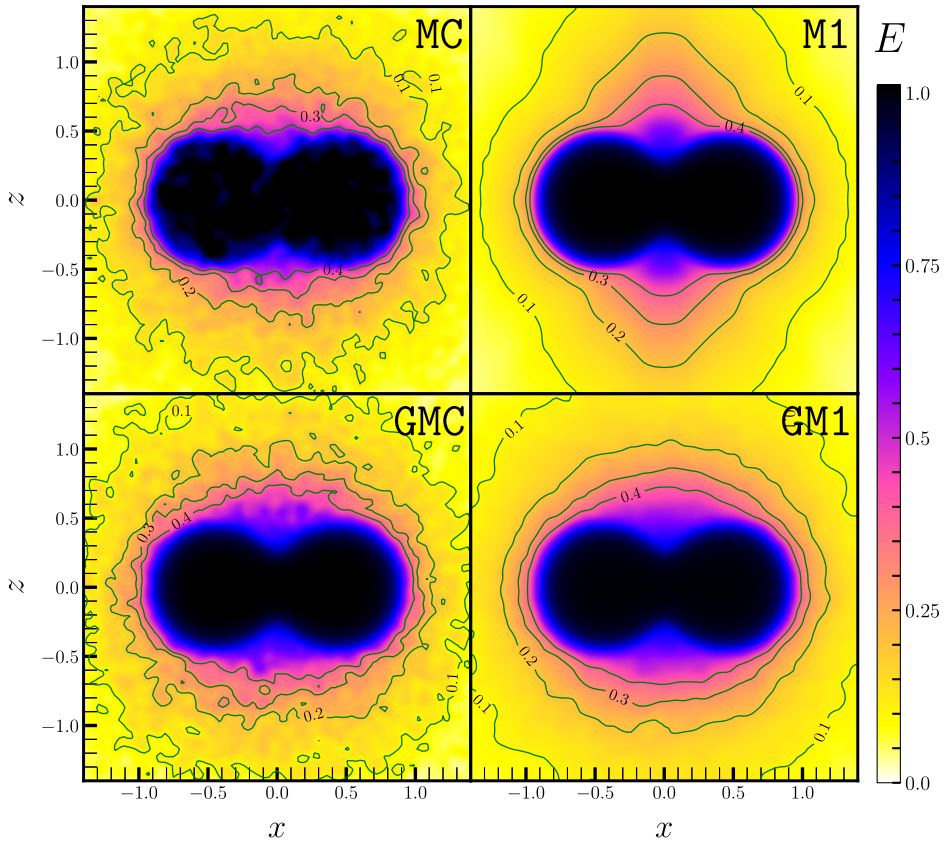

FIG. 14. Radiating and absorbing torus test. The energy density, computed with the MC, M1, GMC, and GM1 schemes using $\Delta x = 0.03$ and $N_{\rm tr} = 40$, is displayed at the meridional plane at time $t = 5$, when the solution has reached a steady state.

the system is better approximated by a torus, which can be described by the following parametric equations in Cartesian coordinates:

$$x(u,v) = (R + r\cos v)\cos u,$$
$$y(u,v) = (R + r\cos v)\sin u,$$
$$z(u,v) = r\sin v.$$

The coordinate position on the torus is determined by the parameters $(u,v) \in [0, 2\pi)$, while the major and minor radii (R, r) define the type of torus. For our specific configuration, we chose a self-intersecting spindle torus (i.e., $r > R$) with $r = 0.5$ and $R = 0.45$. Inside the torus, we again set a high emissivity and absorption opacity $\eta = \kappa_a = 10$, such that neutrinos in this region are in equilibrium with the fluid, representing the optically thick regime. Outside the torus, both the emissivity and absorption opacity are set to zero $\eta = \kappa_a = 0$, modeling an optically thin medium. As the simulation begins, neutrinos emitted from the interior propagate to the exterior. Due to the geometry of the self-intersecting spindle torus, beams will collide along the symmetry axis (i.e., along the $z = 0$ axis), resembling the collision of multiple beams of radiation. The simulation is performed in a three-dimensional Cartesian cubic domain with dimensions $[-3, 3]^3$, employing a fixed spatial resolution $\Delta x = 0.03$ and number of packets $N_{\rm tr} = 40$.

In Fig. 14 we present the final time $t = 5$, when the system has reached a steady state, for the four schemes considered (MC, M1, GMC, GM1). The plot displays a two-dimensional slice along the meridional direction (i.e., the $y = 0$ plane). Similar to the previous test (Sec. IV C), the MC solution appears less smooth due to its intrinsic statistical noise. The crucial distinction between the exact methods and M1 becomes evident when looking along the z axis. In M1, a shock forms where beams collide, representing the previously discussed failure of this approach in the optically thin limit. On the other hand, in the cases of MC, GM1, and GMC, the solutions do not have a large-energy-density region along this axis caused by the artificial collision of radiation. Crucially, our GM formalism, particularly the GM1 solution, exhibits a solution with smoothness comparable to that of M1, but without the presence of shocks. This result confirms and validates the accuracy of the GM method in both the optically thick and thin regimes.

V. CONCLUSIONS

Accurately modeling the intricate physical scenarios within neutron star mergers, especially during the post-merger phase, demands sophisticated numerical simulations. Neutrinos, being crucial contributors to the dynamics and thermodynamics of these events, require a specialized treatment. Here we have introduced a novel approach, the GM formalism, to achieve an accurate and efficient full-neutrino transport treatment in complex environments like neutron star mergers and core-collapse supernovae. This formalism efficiently combines the advantages of the M1 scheme and MC-based methods, providing a robust solution that addresses the strengths and weaknesses of each method.

One of the key concepts in the GM formalism is to compute the closure of the M1 evolution equations (i.e., the second moment) by using information from the MC solution. In the optically thick limit, this closure is analytical and already provides a very accurate and efficient solution. In the same regime, however, the MC scheme has an opposite behavior and faces two challenges: the continuous emission and absorption of neutrino packets and the always present statistical noise associated with stochastic processes. To mitigate these issues, in our GM scheme we use information from the M1 solution to modify the neutrino distribution function such that the MC lowest moments match those evolved by the M1 formalism. On the other hand, the M1 closure in the optically thin limit is not known for multiple sources, so here our GM formalism takes advantage of the cost effectiveness of the MC scheme to compute the exact closure in this regime.

These previous points and the deep discussion included in this paper allow us to say that the GM formalism not only accurately captures the optically thick limit through the exact M1 closure, but also effectively resolves the optically thin limit, which is a known challenge for the M1 approach but accurately handled by MC methods. The resulting scheme outperforms both the M1 and MC approaches, providing a comprehensive and accurate solution in both regimes. Although we have focused on the pressure tensor closure, our method likely also improves the energy closure. Studying this issue is beyond the scope of this paper, but it will be thoroughly discussed in future work involving astrophysical scenarios.

The detailed exposition of the GM formalism, its formulation, and implementation, along with a thorough comparison with M1 and MC methods across various test problems, demonstrates the efficacy of the proposed approach. The computational cost of evolving the MC solution in optically thick regions can be substantial in real simulations. This issue can be mitigated within the GM scheme by effectively limiting the emissivities and opacities only in the MC scheme for these regions, thereby reducing the overall computational cost. As there is a complete matching of the lowest moments of M1 and those of MC, there should not be any degradation of the accuracy in the GM solution.

Another potential improvement is related to modifying the matching function $h(\xi)$ [see Eq. (43) and Fig. 1], which determines the regime in which we will match the lowest moments calculated with the M1 solution with those obtained from the MC scheme. While the presented test problems show promising behavior, fine-tuning might be

necessary in more realistic simulations and will probably require a more careful exploration.

ACKNOWLEDGMENTS

We thank Federico Carrasco, Lorenzo Pareschi, and David Radice for suggestions and clarifications on the subjects of this work. M. R. I. is grateful for the hospitality and stimulating discussions during his visit at Stony Brook's Physics and Astronomy Department and at the Institute for Gravitation and the Cosmos (Penn State University). C. P. acknowledges the hospitality at the Institute for Pure & Applied Mathematics through the Long Program "Mathematical and Computational Challenges in the Era of Gravitational Wave Astronomy," where this project was initiated. M. R. I. thanks the financial support of grant PRE2020-094166 funded by the Ministerio de Ciencia e Innovación/Agencia Estatal de Investigación (MCIN/AEI/PID2019–110301GB-I00) and by "FSE invierte en tu futuro." This work was supported by the grants PID2022-138963NB-I00 and PID2019–110301GB-I00 funded by MCIN/AEI/10.13039/501100011033 and by "ERDF A way of making Europe."

APPENDIX A: MATCHING THE NEUTRINO NUMBER DENSITY

Recent extensions of the M1 formalism (see, e.g., [53,57,58]) also evolve the number density of neutrinos. Notice that, without evolving the number density, the M1 formalism with the grey approximation does not accurately conserve the lepton number [53]. Although this issue might not be so dramatic in the GM approach, where there is a better estimate of the neutrino energy spectrum, it might still be problematic. To this aim, for each neutrino species one can introduce a neutrino number current N^a following a conservation equation,

$$\nabla_a N^a = \sqrt{-g}\mathcal{C} = \sqrt{-g}(\eta^0 - \kappa_a^0 n), \tag{A1}$$

where $n = -N^a u_a$ is the neutrino density in the fluid frame and (κ_a^0, η^0) are the neutrino number absorption and emission coefficients, which also need to be computed from the fluid state and the information in the equation-of-state tables.

Assuming that the neutrino number density and the radiation flux are aligned, this equation can be written in the $3+1$ decomposition as

$$\partial_t(\sqrt{\gamma}N) + \partial_k\left[\sqrt{\gamma}\left(-W\beta^k + \alpha W v^k + \alpha\frac{H^k}{J}\right)\frac{N}{\Gamma}\right] = \alpha\sqrt{\gamma}\left(\eta^0 - \kappa_a^0\frac{N}{\Gamma}\right), \tag{A2}$$

where $N = -n_a N^a = n\Gamma$ is the neutrino density in the inertial frame and

$$\Gamma = W - \frac{1}{J}H^a n_a = W\left(\frac{E - F_a v^a}{J}\right). \tag{A3}$$

Within this new equation, one can dynamically estimate the average energy of the neutrinos ϵ_ν, since in the fluid frame the relation $J \approx n\langle\epsilon_\nu\rangle$ is approximately satisfied.

In the GM formalism we are matching the lowest moments, but it might also be desirable to match the neutrino number density if it is also being evolved in M1.

It is straightforward to show that, in the discrete packet distribution, the neutrino number density and the lowest moments, measured in the grid frame, can just be computed as

$$\bar{N} = \sum_{k\in\Delta V}\frac{N_k}{\sqrt{\gamma}\Delta V}, \qquad \bar{\mathcal{J}}_a = \sum_{k\in\Delta V} N_k\frac{p_a^k}{\sqrt{\gamma}\Delta V}. \tag{A4}$$

The first step is to match the neutrino number density $\bar{N}$ to N, a task that requires a modification of the weights N_k. This can be achieved by performing the simple renormalization

$$\tilde{N}_k \equiv \frac{N}{\bar{N}}N_k \to N = \sum_{k\in\Delta V}\frac{\tilde{N}_k}{\sqrt{\gamma}\Delta V}, \tag{A5}$$

which implies that the projection of the stress-energy tensor now needs to be computed as

$$\bar{\mathcal{J}}_a = \sum_{k\in\Delta V}\tilde{N}_k\frac{p_a^k}{\sqrt{\gamma}\Delta V}. \tag{A6}$$

Basically, the interpretation of this new relation for the moments is that changing the number of neutrinos in a cell automatically changes the energy and flux densities in that cell.

The rest of the procedure for matching moments remains the same, such that the final result

$$\mathcal{J}^b = \sum_{k\in\Delta V}\tilde{N}_k\frac{\tilde{p}_b^k}{\sqrt{\gamma}\Delta V} \tag{A7}$$

now involves two transformations: changing $N_k \to \tilde{N}_k$ (i.e., modifying the weights such that the densities of neutrinos are equal) and $p_b^k \to \tilde{p}_b^k$ (i.e., modifying the neutrino 4-momentum such that the lowest moments match).

APPENDIX B: TETRAD

Two special observers play an important role in the description of our neutrino transport algorithm: inertial observers, whose timeline is tangent to n^a, and comoving observers, whose timeline is tangent to u^a.

Our numerical grid is discretized in the spatial coordinates x^i. We refer to the coordinates (t, x^i) as the inertial or grid frame, where the line element is

$$ds^2 = g_{ab}dx^a dx^b. \tag{B1}$$

We also define the coordinates of the fluid rest frame $(t', x^{i'})$, which are defined at a point such that

$$ds^2 = \eta_{a'b'}dx^{a'}dx^{b'}, \tag{B2}$$

where $\eta_{a'b'}$ is the Minkowski metric and $(t')^a = u^a$. We construct these local coordinates from an orthonormal tetrad $e_a^{(c')}$, with

$$\hat{e}^a_{(t')} = u^a, \tag{B3}$$

$$g^{ab}\hat{e}_a^{(c')}\hat{e}_b^{(d')} = \eta^{c'd'}. \tag{B4}$$

The three other components of the tetrad are obtained by applying the Gram-Schmidt algorithm to the three vectors $V^a_{(i)} = \delta^a_i$ $(i = 1, 2, 3)$. The orthonormal tetrad $\hat{e}^a_{(c')}$ and the corresponding 1-forms $\hat{e}_a^{(c')}$ are precomputed and stored for each grid cell at each time step, and can be used to easily perform transformations from the fluid rest frame coordinates to grid coordinates (and vice versa) by simple matrix-vector multiplication.

In order to convert the 4-momentum from the lab frame $(\mathcal{S})$ to the fluid rest frame or comoving frame $(\mathcal{S}')$, we need to find a basis that relates p^c and $p^{c'}$. This will be necessary when initializing the packets (set random moments), after scattering (redraw momentum), and when packets are emitted (new initialization). In these simulations, the momentum is drawn from a spherical uniform distribution, i.e.,

$$p^{c'} = \nu(1, \sin\theta\cos\phi, \sin\theta\sin\phi, \cos\theta). \tag{B5}$$

We draw $\cos(\theta)$ from a uniform distribution in $[-1, 1]$ and ϕ from a uniform distribution in $[0, 2\pi]$. The 4-momentum of neutrinos in grid coordinates can then be computed using the transformation

$$p^t = \hat{e}^t_{(c')}p^{c'}, \tag{B6}$$

$$p_i = g_{ia}\hat{e}^a_{(c')}p^{c'} = \delta_{c'd'}\hat{e}_i^{(c')}p^{d'}. \tag{B7}$$

[1] B. P. Abbott, R. Abbott, T. D. Abbott, F. Acernese, K. Ackley, C. Adams, T. Adams, P. Addesso, R. X. Adhikari, V. B. Adya, C. Affeldt, M. Afrough, B. Agarwal, M. Agathos, K. Agatsuma, and N. Aggarwal, Astrophys. J. Lett. **848**, L12 (2017).
[2] B. P. Abbott *et al.* (LIGO Scientific and Virgo Collaborations), Phys. Rev. Lett. **119**, 161101 (2017).
[3] A. Colombo, O. S. Salafia, F. Gabrielli, G. Ghirlanda, B. Giacomazzo, A. Perego, and M. Colpi, Astrophys. J. **937**, 79 (2022).
[4] K. Kiuchi, K. Kyutoku, Y. Sekiguchi, and M. Shibata, Phys. Rev. D **97**, 124039 (2018).
[5] F. Foucart, Living Rev. Comput. Astrophys. **9**, 1 (2023).
[6] J. Lippuner and L. F. Roberts, Astrophys. J. **815**, 82 (2015).
[7] O. Just, A. Bauswein, R. A. Pulpillo, S. Goriely, and H.-T. Janka, Mon. Not. R. Astron. Soc. **448**, 541 (2015).
[8] F.-K. Thielemann, M. Eichler, I. Panov, and B. Wehmeyer, Annu. Rev. Nucl. Part. Sci. **67**, 253 (2017).
[9] A. Perego, F. K. Thielemann, and G. Cescutti, *r*-process nucleosynthesis from compact binary mergers, in *Handbook of Gravitational Wave Astronomy* (Springer Singapore, Singapore, 2020), pp. 1–56.
[10] L. Dessart, C. D. Ott, A. Burrows, S. Rosswog, and E. Livne, Astrophys. J. **690**, 1681 (2008).
[11] A. Perego, S. Rosswog, R. M. Cabezon, O. Korobkin, R. Kappeli, A. Arcones, and M. Liebendorfer, Mon. Not. R. Astron. Soc. **443**, 3134 (2014).
[12] S. Fujibayashi, Y. Sekiguchi, K. Kiuchi, and M. Shibata, Astrophys. J. **846**, 114 (2017).
[13] S. Fujibayashi, S. Wanajo, K. Kiuchi, K. Kyutoku, Y. Sekiguchi, and M. Shibata, Astrophys. J. **901**, 122 (2020).
[14] F. Foucart, P. Laguna, G. Lovelace, D. Radice, and H. Witek, arXiv:2203.08139.
[15] E. Abdikamalov, A. Burrows, C. D. Ott, F. Löffler, E. O'Connor, J. C. Dolence, and E. Schnetter, Astrophys. J. **755**, 111 (2012).
[16] S. Richers, D. Kasen, E. O'Connor, R. Fernández, and C. D. Ott, Astrophys. J. **813**, 38 (2015).
[17] B. R. Ryan, J. C. Dolence, and C. F. Gammie, Astrophys. J. **807**, 31 (2015).
[18] F. Foucart, Mon. Not. R. Astron. Soc. **475**, 4186 (2018).
[19] F. Foucart, M. D. Duez, L. E. Kidder, R. Nguyen, H. P. Pfeiffer, and M. A. Scheel, Phys. Rev. D **98**, 063007 (2018).
[20] B. R. Ryan and J. C. Dolence, Astrophys. J. **891**, 118 (2020).
[21] F. Foucart, M. D. Duez, F. Hébert, L. E. Kidder, P. Kovarik, H. P. Pfeiffer, and M. A. Scheel, Astrophys. J. **920**, 82 (2021).
[22] K. Kawaguchi, S. Fujibayashi, and M. Shibata, Phys. Rev. D **107**, 023026 (2023).
[23] F. Foucart, M. D. Duez, R. Haas, L. E. Kidder, H. P. Pfeiffer, M. A. Scheel, and E. Spira-Savett, Phys. Rev. D **107**, 103055 (2023).
[24] L. R. Weih, A. Gabbana, D. Simeoni, L. Rezzolla, S. Succi, and R. Tripiccione, Mon. Not. R. Astron. Soc. **498**, 3374 (2020).
[25] G. Pomraning, *The Equations of Radiation Hydrodynamics*, International Series of Monographs in Natural Philosophy (Pergamon Press, Oxford, UK, 1973).

[26] R. G. McClarren and C. D. Hauck, J. Comput. Phys. **229**, 5597 (2010).
[27] D. Radice, E. Abdikamalov, L. Rezzolla, and C. D. Ott, J. Comput. Phys. **242**, 648 (2013).
[28] G. C. Pomraning, J. Quant. Spectrosc. Radiat. Transfer **9**, 407 (1969).
[29] D. Mihalas and B. Weibel-Mihalas, *Foundations of Radiation Hydrodynamics* (Dover Publications, Mineola, NY, USA, 1999).
[30] C. Chan and B. Müller, Mon. Not. R. Astron. Soc. **496**, 2000 (2020).
[31] M. K. Bhattacharyya and D. Radice, J. Comput. Phys. **491**, 112365 (2023).
[32] J. Fleck and J. Cummings, J. Comput. Phys. **8**, 313 (1971).
[33] J. Fleck and E. Canfield, J. Comput. Phys. **54**, 508 (1984).
[34] A. B. Wollaber, Advanced Monte Carlo methods for thermal radiation transport, Ph.D. thesis, University of Michigan, 2008.
[35] S. Richers, H. Nagakura, C. D. Ott, J. Dolence, K. Sumiyoshi, and S. Yamada, Astrophys. J. **847**, 133 (2017).
[36] M. Ruffert, H. T. Janka, and G. Schaefer, Astron. Astrophys. **311**, 532 (1996).
[37] S. Rosswog and M. Liebendörfer, Mon. Not. R. Astron. Soc. **342**, 673 (2003).
[38] Y. Sekiguchi, Classical Quantum Gravity **27**, 114107 (2010).
[39] D. Neilsen, S. L. Liebling, M. Anderson, L. Lehner, E. O'Connor, and C. Palenzuela, Phys. Rev. D **89**, 104029 (2014).
[40] C. Palenzuela, S. L. Liebling, D. Neilsen, L. Lehner, O. L. Caballero, E. O'Connor, and M. Anderson, Phys. Rev. D **92**, 044045 (2015).
[41] A. Perego, R. M. Cabezón, and R. Käppeli, Astrophys. J. Suppl. Ser. **223**, 22 (2016).
[42] E. R. Most, L. J. Papenfort, and L. Rezzolla, Mon. Not. R. Astron. Soc. **490**, 3588 (2019).
[43] C. Palenzuela, S. Liebling, and B. Miñano, Phys. Rev. D **105**, 103020 (2022).
[44] K. S. Thorne, Mon. Not. R. Astron. Soc. **194**, 439 (1981).
[45] M. Shibata, K. Kiuchi, Y. Sekiguchi, and Y. Suwa, Prog. Theor. Phys. **125**, 1255 (2011).
[46] A. Sadowski, R. Narayan, A. Tchekhovskoy, and Y. Zhu, Mon. Not. R. Astron. Soc. **429**, 3533 (2013).
[47] J. C. McKinney, A. Tchekhovskoy, A. Sadowski, and R. Narayan, Mon. Not. R. Astron. Soc. **441**, 3177 (2014).
[48] S. Wanajo, Y. Sekiguchi, N. Nishimura, K. Kiuchi, K. Kyutoku, and M. Shibata, Astrophys. J. Lett. **789**, L39 (2014).
[49] F. Foucart, E. O'Connor, L. Roberts, M. D. Duez, R. Haas, L. E. Kidder, C. D. Ott, H. P. Pfeiffer, M. A. Scheel, and B. Szilagyi, Phys. Rev. D **91**, 124021 (2015).
[50] O. Just, M. Obergaulinger, and H.-T. Janka, Mon. Not. R. Astron. Soc. **453**, 3387 (2015).
[51] Y. Sekiguchi, K. Kiuchi, K. Kyutoku, and M. Shibata, Phys. Rev. D **91**, 064059 (2015).
[52] T. Kuroda, T. Takiwaki, and K. Kotake, Astrophys. J. Suppl. Ser. **222**, 20 (2016).
[53] F. Foucart, E. O'Connor, L. Roberts, L. E. Kidder, H. P. Pfeiffer, and M. A. Scheel, Phys. Rev. D **94**, 123016 (2016).
[54] M. A. Skinner, J. C. Dolence, A. Burrows, D. Radice, and D. Vartanyan, Astrophys. J. Suppl. Ser. **241**, 7 (2019).
[55] J. D. M. Fuksman and A. Mignone, Astrophys. J. Suppl. Ser. **242**, 20 (2019).
[56] L. R. Weih, H. Olivares, and L. Rezzolla, Mon. Not. R. Astron. Soc. **495**, 2285 (2020).
[57] D. Radice, S. Bernuzzi, A. Perego, and R. Haas, Mon. Not. R. Astron. Soc. **512**, 1499 (2022).
[58] M. R. Izquierdo, L. Pareschi, B. Miñano, J. Massó, and C. Palenzuela, Classical Quantum Gravity **40**, 145014 (2023).
[59] P. C.-K. Cheong, H. H.-Y. Ng, A. T.-L. Lam, and T. G. F. Li, Astrophys. J. Suppl. Ser. **267**, 38 (2023).
[60] C. Musolino and L. Rezzolla, arXiv:2304.09168.
[61] F. Schianchi, H. Gieg, V. Nedora, A. Neuweiler, M. Ujevic, M. Bulla, and T. Dietrich, arXiv:2307.04572.
[62] U. M. Ascher, S. J. Ruuth, and R. J. Spiteri, Appl. Numer. Math. **25**, 151 (1997).
[63] L. Pareschi and G. Russo, Implicit-explicit Runge-Kutta schemes for stiff systems of differential equations, in *Recent Trends in Numerical Analysis* (Nova Science Publishers, Inc., USA, 2000), pp. 269–288.
[64] C. A. Kennedy and M. H. Carpenter, Appl. Numer. Math. **44**, 139 (2003).
[65] L. Pareschi and G. Russo, J. Sci. Comput. **25**, 129 (2005).
[66] P. Degond, G. Dimarco, and L. Pareschi, Int. J. Numer. Methods Fluids **67**, 189 (2011).
[67] G. Dimarco, Kinet. Relat. Models **6**, 291 (2013).
[68] C. D. Levermore and G. C. Pomraning, Astrophys. J. **248**, 321 (1981).
[69] G. Minerbo, Comput. Graphics Image Process. **10**, 48 (1979).
[70] E. M. Murchikova, E. Abdikamalov, and T. Urbatsch, Mon. Not. R. Astron. Soc. **469**, 1725 (2017).
[71] Z. Oziewicz, arXiv:math-ph/0608062.
[72] E. Celakoska, D. Chakmakov, and M. Petrushevski, Int. J. Contemp. Math. Sci. **10**, 85 (2015).
[73] C. D. Levermore, J. Quant. Spectrosc. Radiat. Transfer **31**, 149 (1984).
[74] J. M. Smit, J. Cernohorsky, and C. P. Dullemond, Astron. Astrophys. **325**, 203 (1997).
[75] J. A. Pons, J. M. Ibanez, and J. A. Miralles, Mon. Not. R. Astron. Soc. **317**, 550 (2000).
[76] M. Rampp and H. T. Janka, Astron. Astrophys. **396**, 361 (2002).
[77] D. Radice, E. Abdikamalov, L. Rezzolla, and C. D. Ott, J. Comput. Phys. **242**, 648 (2013).
[78] P. Anninos and P. C. Fragile, Astrophys. J. **900**, 71 (2020).
[79] C. Chan and B. Müller, Mon. Not. R. Astron. Soc. **496**, 2000 (2020).